JOURNAL OF GEOPHYSICAL RESEARCH, VOL. 105, NO. B7, PAGES 16,303–16,327, JULY 10, 2000

Dating of major normal fault systems using thermochronology: An example from the Raft River detachment, Basin and Range, western United States

Michael L. Wells

Department of Geoscience, University of Nevada, Las Vegas

Lawrence W. Snee

U.S. Geological Survey, Denver, Colorado

Ann E. Blythe

Department of Earth Sciences, University of Southern California, Los Angeles

Abstract. Application of thermochronological techniques to major normal fault systems can resolve the timing of initiation and duration of extension, rates of motion on detachment faults, timing of ductile mylonite formation and passage of rocks through the crystal-plastic to brittle transition, and multiple events of extensional unroofing. Here we determine the above for the top-to-the-east Raft River detachment fault and shear zone by study of spatial gradients in $^{40}Ar/^{39}Ar$ and fission track cooling ages of footwall rocks and cooling histories and by comparison of cooling histories with deformation temperatures. Mica $^{40}Ar/^{39}Ar$ cooling ages indicate that extension-related cooling began at ~25-20 Ma, and apatite fission track ages show that motion on the Raft River detachment proceeded until ~7.4 Ma. Collective cooling curves show acceleration of cooling rates during extension, from 5-10°C/m.y. to rates in excess of 70-100°C/m.y. The apparent slip rate along the Raft River detachment, recorded in spatial gradients of apatite fission track ages, is 7 mm/yr between 13.5 and 7.4 Ma and is interpreted to record the rate of migration of a rolling hinge. Microstructural study of footwall mylonite indicates that deformation conditions were no higher than middle greenschist facies and that deformation occurred during cooling to cataclastic conditions. These data show that the shear zone and detachment fault represent a continuum produced by progressive exhumation and shearing during Miocene extension and preclude the possibility of a Mesozoic age for the ductile shear zone. Moderately rapid cooling in middle Eocene time likely records exhumation resulting from an older, oppositely rooted, extensional shear zone along the west side of the Grouse Creek, Raft River, and Albion Mountains.

1. Introduction

Determining the absolute age of deformation events is commonly a difficult aspect of structural studies. Particularly problematic is dating deformations whose geologic structures lack cross cutting or bracketing igneous and sedimentary rocks, lack syntectonic sedimentary records, and deform rocks significantly older than the deformation (e.g., dating a Miocene deformation event in Precambrian rocks). In this paper, we determine the timing of deformation along a shear zone and detachment fault in a Cordilleran metamorphic core complex, the Raft River Mountains of northwestern Utah (Figure 1), by $^{40}Ar/^{39}Ar$ and fission track thermochronology of footwall rocks. First, we use the spatial gradient in cooling ages to establish the timing of initial motion of the hanging wall block relative to the footwall. Second, we integrate the cooling history determined from $^{40}Ar/^{39}Ar$ and fission track thermochronology with the temperature conditions of deformation, inferred from study of deformation mechanisms, to further constrain the age and extensional origin for the shear zone. This is of significance because the shear zone has been alternatively interpreted as the deep level of a Cenozoic normal fault [*Malavieille*, 1987; *Manning and Bartley*, 1994], Mesozoic thrust [e.g., *Malavieille and Cobb*, 1986; *Sabisky*, 1985; *Snoke and Miller*, 1988], or a Mesozoic thrust overprinted by a Cenozoic normal fault [*Crittenden*, 1979].

The Raft River Mountains expose an Archean basement complex dominated by Archean monzogranite, unconformably overlain by a Proterozoic sequence of alternating quartzite and schist (Figures 1, 2, and 3). A ductile shear zone and overlying brittle fault are located along and above the unconformity. The stratigraphic and structural level of this decollement is compatible with a Mesozoic contractional decollement localized at the base of the miogeoclinal sedimentary prism because of similarity in the position of the basal decollement inferred from the oldest rocks in thrust sheets to the east [*Crittenden*, 1979] and because the unconformity represents a significant rheologic boundary [*Wells and Struthers*, 1995]. Additionally, the translation

Paper number 2000JB900094.
0148-0227/00/2000JB900094$09.00

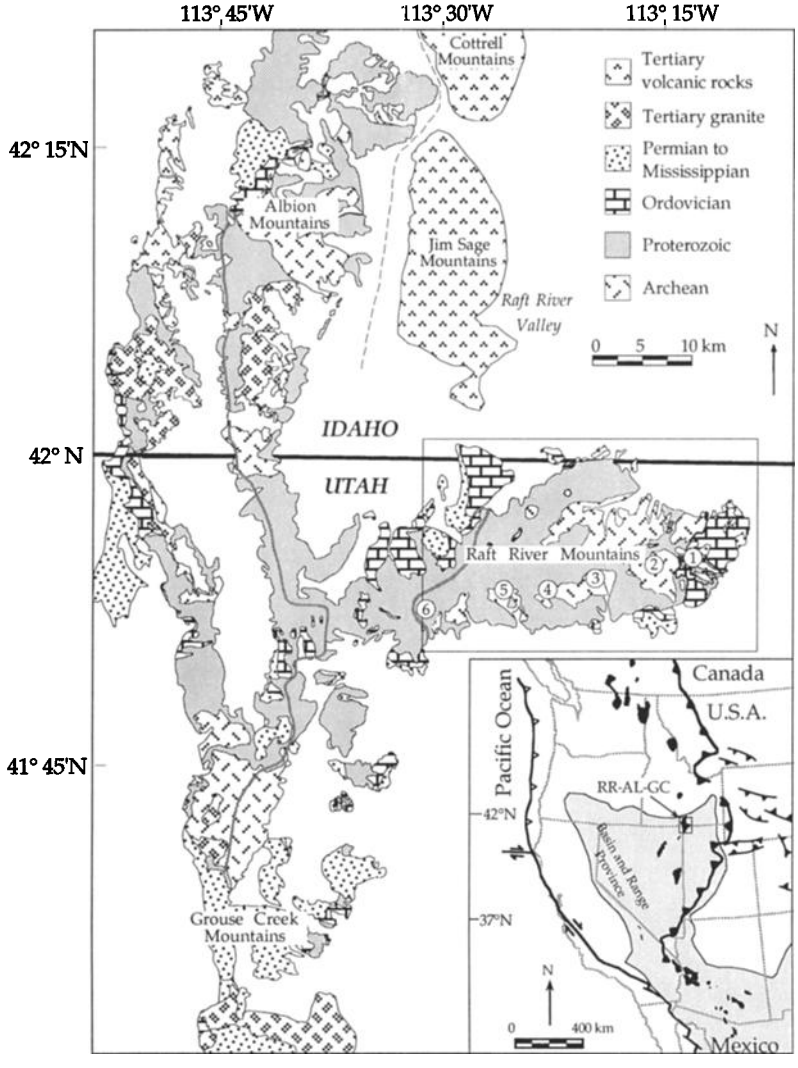

Figure 1. Simplified geologic and sample location map of the Raft River Mountains and parts of Albion and Grouse Creek Mountains. Light shaded line in the Albion, western Raft River, and Grouse Creek Mountains is the approximate eastern boundary (footwall cutoff) of the top-to-the-WNW Middle Mountain shear zone in the Elba Quartzite; thicker shaded line in central Raft River Mountains is the western boundary of the Miocene top-to-the-east Raft River shear zone in the Elba Quartzite. Box in eastern Raft River Mountains indicates location of more detailed geologic map of Figure 2. Modified from *Compton* [1972, 1975], *Armstrong et al.* [1978], *Todd* [1980], and *Wells* [1996]. Sample locations for $^{40}Ar/^{39}Ar$ and fission track thermochronology are indicated by number: 1, Ten Mile Canyon: 2, Indian Creek Canyon; 3, Dunn Creek Canyon; 4, Fisher Creek Canyon; 5, Pine Creek Canyon; 6, Century Hollow; 7, Clarks Basin; and 8, Kimbell Creek. Inset shows generalized location and tectonic map of western North America, illustrating locations of Basin and Range Province (shaded pattern), metamorphic core complexes (solid areas), leading edge of Sevier fold and thrust belt (thick barbed line), and Raft River-Albion- Grouse Creek metamorphic core complex (RR-AL-GC), and present plate boundaries.

direction determined from studies of the shear zone is compatible with eastward thrusting as documented in the foreland fold and thrust belt [*Malavieille and Cobb*, 1986; *Sabisky*, 1985]. Stratigraphic studies and seismic reflection and drill hole data from the Raft River Valley (Figure 1). however, have shown that the brittle detachment fault displaces rocks as young as Miocene and have led to the interpretation that the brittle detachment fault and underlying shear zone are of Miocene age and extensional origin [*Williams et al.*, 1982; *Covington*, 1983; *Malavieille*, 1987]. It is difficult to date the shear zone directly because of the lack and scarcity of Mesozoic and Cenozoic intrusive rocks, respectively, and because the youngest rocks deformed by the shear zone are Proterozoic in age. Therefore, despite the evidence for a Miocene age for last movement on the brittle fault, the underlying ductile shear zone may be a distinctly older structure. Such conservatism in interpretation is warranted because early higher-temperature shear zones can be reactivated during lower-temperature shearing of significantly younger age [e.g., *Applegate et al.*, 1992]; this is the case for the west rooted Middle Mountain shear zone that bounds the tract of metamorphic rocks along its western flank (Figure 1) [*Saltzer and Hodges*, 1988; *Wells et al.*, 1997b]. New geologic and thermochronologic data from the eastern and

central Raft River Mountains, presented here, corroborate the interpretation that the Raft River detachment and footwall shear zone record Miocene extension [*Covington*, 1983] and indicate that the shear zone and detachment fault represent a continuum produced by progressive exhumation and shearing during Miocene extension.

2. Raft River Detachment and Shear Zone

The Raft River, Albion, and Grouse Creek Mountains expose amphibolite to greenschist facies metamorphic rocks of Archean to Permian age that record burial by thrusting within the hinterland of the Mesozoic to early Cenozoic Sevier orogen. These mountains comprise one of the isolated exposures of metamorphic core complexes that form a north trending belt in the Cordillera of the western United States [e.g., *Crittenden et al.*, 1980] (Figure 1). Metamorphic core complexes typically exhibit a hanging wall of younger and lesser metamorphosed rocks juxtaposed across a detachment fault from older footwall rocks of higher metamorphic grade or greater preextensional structural depth. Metamorphic core complexes have been interpreted as products of marked and localized continental extension that was driven in part by gravitational potential energy resulting from earlier crustal thickening [*Coney and Harms*, 1984], the later of which is not always well displayed. Late Mesozoic to early Cenozoic ductile structures and metamorphic rocks in the Raft River-Albion-Grouse Creek metamorphic core complex were exhumed along two oppositely rooted Cenozoic detachment fault and shear zone systems: a west rooted middle Eocene to early Oligocene shear zone exposed in the Grouse Creek and western Raft River and Albion Mountains that was reactivated in the Miocene [*Compton*, 1983; *Saltzer and Hodges*, 1988; *Wells et al.*, 1997b] and the east rooted Raft River detachment fault and shear zone present in the central and eastern Raft River Mountains [*Malavieille*, 1987] (Figure

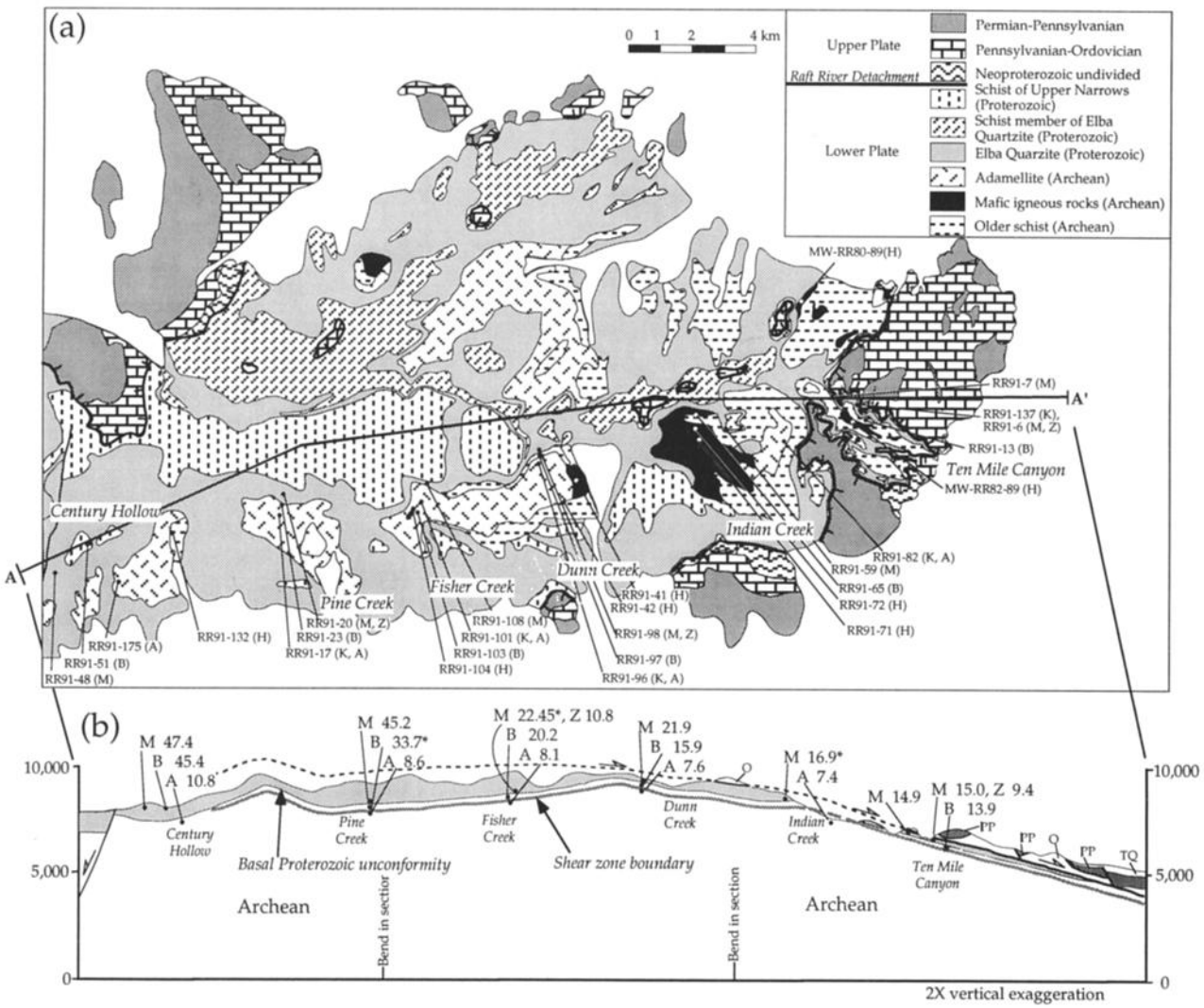

Figure 2. (a) Geologic and sample location map of the eastern and central Raft River Mountains, simplified from *Compton* [1972, 1975] and *Wells* [1996]. Sample numbers and locations are indicated; H, hornblende; M, muscovite; B, biotite; K, K-feldspar; A, apatite; Z, zircon. (b) Geologic cross section of the Raft River Mountains, parallel to the transport direction of the shear zone and detachment fault, showing sample locations and $^{40}Ar/^{39}Ar$ and fission track cooling ages. Mineral abbreviations are same as in Figure 2a. All mica $^{40}Ar/^{39}Ar$ ages are preferred ages, except those with asterisk, which are total gas ages.

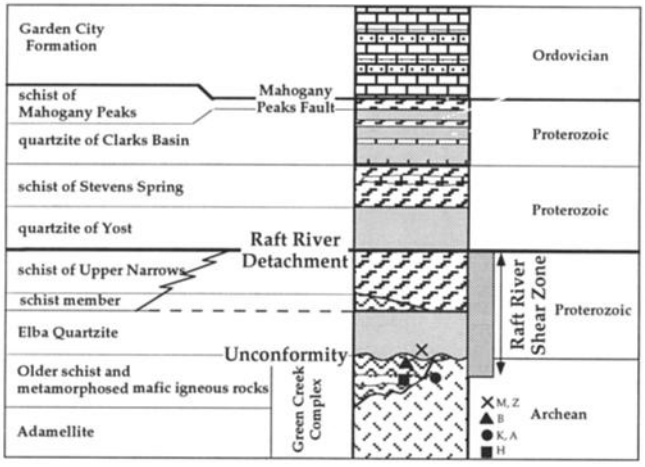

Figure 3. Simplified columnar section of Ordovician and older rocks of the Raft River Mountains. The Raft River shear zone is positioned within Proterozoic rocks beneath the Raft River detachment and within the uppermost few to tens of meters of Archean rocks beneath the basement unconformity. Locations of thermochronology samples are shown and labeled as follows: M, muscovite; B, biotite; K, K-feldspar; H, hornblende; A, apatite; Z, zircon.

1). The oppositely vergent shear zone systems that bound the metamorphic core have been interpreted as being simultaneously active, and a type example of symmetric bivergent extention [e.g., *Malavieille*, 1993].

The eastern and central Raft River Mountains expose the Raft River detachment fault, which separates a hanging wall composed of Proterozoic and Paleozoic strata from a footwall of Archean and Proterozoic rocks [*Compton et al.*, 1977; *Malavieille*, 1987; *Wells*, 1997] (Figures 1, 2, and 3). The detachment fault caps a 100- to 300-m-thick shear zone, developed within a Proterozoic metasedimentary sequence and the top few to tens of meters of an unconformably underlying Archean basement complex (Green Creek Complex of *Armstrong*, [1968]). The Green Creek Complex is composed of ~2.5 Ga gneissic monzogranite and its intruded country rocks of schist, trondhjemite and amphibolite [*Compton*, 1975; *Compton et al.*, 1977]. These Archean rocks are nonconformably overlain by the Proterozoic Elba Quartzite and overlying schist and quartzite (Figures 2 and 3). The Raft River detachment everywhere overlies the schist member of the Elba Quartzite in the eastern Raft River Mountains and the schist of Upper Narrows, of probable stratigraphic equivalence, in the central part of the range [*Compton*, 1975; *Compton et al.*, 1977; *Wells*, 1996, 1997] (Figures 2 and 3).

Mylonitic fabrics of the Raft River shear zone are most highly developed within the Elba Quartzite and overlying schist, and fabric intensity related to eastward shearing typically dies out abruptly downward within the Green Creek Complex. Kinematic studies of the plastic shear zone consistently indicate a significant component of noncoaxial top-to-the-east shearing [*Compton*, 1980; *Sabisky*, 1985; *Malavieille*, 1987; *Wells*, 1997] (Figure 4). There is a close spatial and kinematic association between the shear zone and the overlying detachment fault. The mylonitic rocks are progressively overprinted by cataclastic deformation structurally upward toward the detachment fault. Both cataclasites and mylonites exhibit the same top-to-the-east shear sense.

Microstructural observations and quartz slip system inferences from lattice-preferred orientations are consistent with greenschist facies metamorphic conditions and ductile shearing during decreasing temperature. Quartz microstructures exhibit many unrecovered deformation features indicative of low-temperature plasticity. Deformation lamellae of subbasal orientation are common (Figure 5a) [see also *Compton*, 1980]. Deformation lamellae have been described from various naturally occurring quartzite tectonites and are associated with high differential stresses and relatively low temperatures [*White*, 1973; *Law*, 1990]. Optically visible offset of grain boundaries along some of the Raft River deformation lamellae implies that some represent dislocation glide planes accommodating subbasal <*a*> slip. Other low-temperature quartzite microstructures include subgrain development, deformation bands, and undulatory extinction (Figure 5b). Quartz *c* axis lattice-preferred orientations show asymmetric crossed girdles and single girdles [*Compton*, 1980; *Sabisky*, 1985; *Malavieille*, 1987] (Figure 4) with maxima consistent with primarily basal slip in <*a*> with subordinate rhomb and prism slip in <*a*> [*Schmid and Casey*, 1986]. Deformation of K-feldspar is restricted to mechanisms of brittle fracturing and slip along cleavage surfaces (Figure 5c). Tensile fractures oriented perpendicular to foliation and lineation are infilled with quartz which in some cases exhibit elongate grains

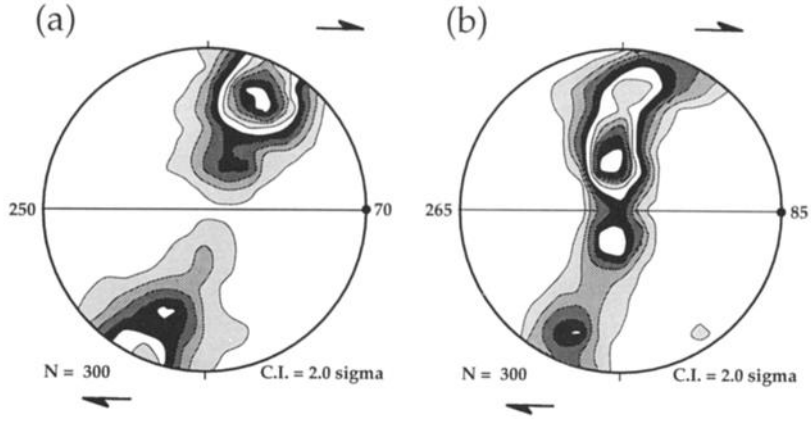

Figure 4. Representative quartz lattice-preferred orientations from the Raft River shear zone. The E-W great circle represents the macroscopic foliation plane; solid circle indicates lineation. (a) West end of shear zone, Century Hollow. (b) East end, Indian Creek.

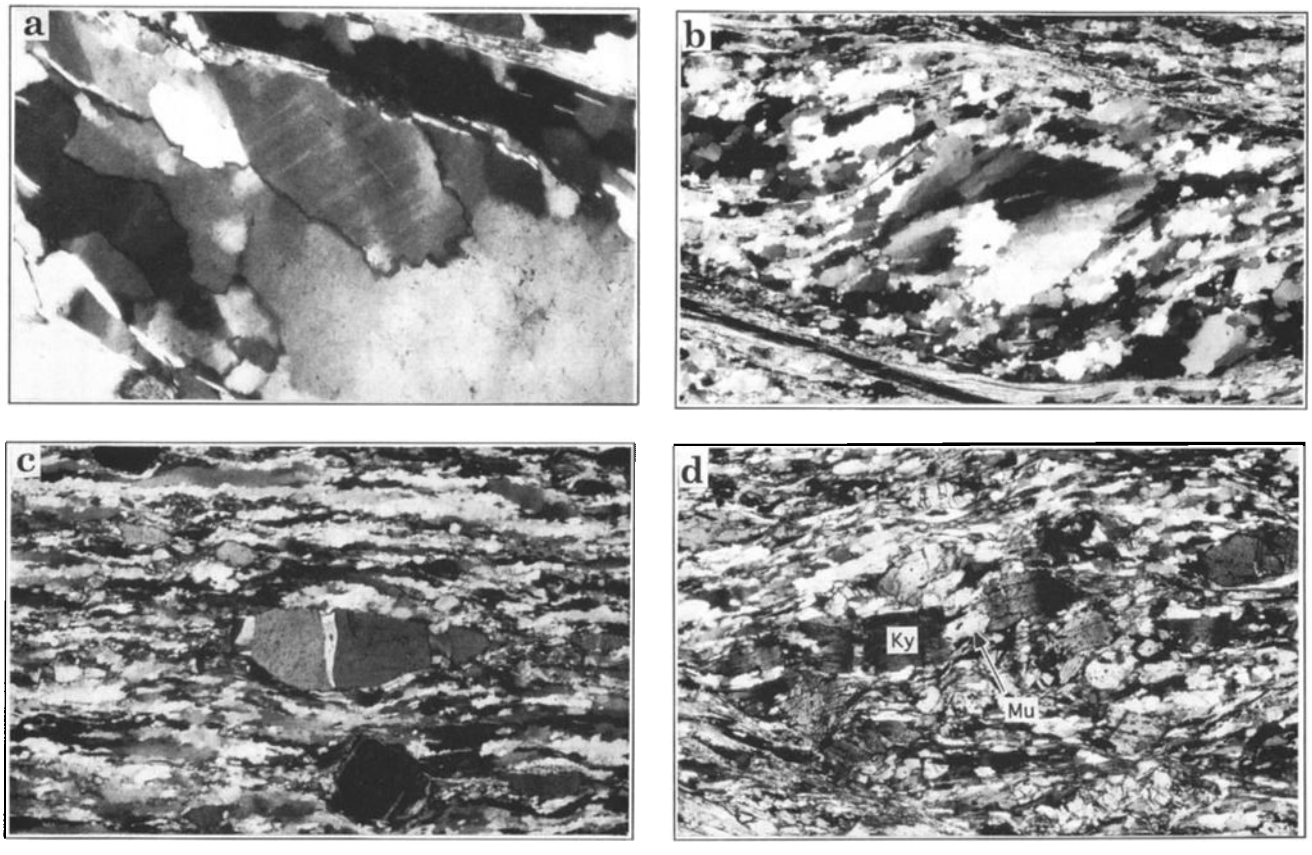

Figure 5. Photomicrographs of deformation microstructures from Elba Quartzite within the Raft River shear zone. All sections are parallel to lineation and perpendicular to foliation. (a) Deformation lamellae in quartz. Note boudinaged rutile needles in center of view that transect new grain boundary formed by grain boundary migration recrystallization. Field of view is 670 μm. (b) Dynamically recrystallized large quartz grain. Note deformation bands and subgrains in core of grain and new grains within mantle. Obliquity of elongate dynamically recrystallized quartz relative to bounding shear bands and asymmetry of relict quartz grain indicate dextral shearing. Field of view is 3.3 mm. (c) Extension fractures of feldspar porphyroclast, filled by quartz with sparse relict fibers, suggesting pressure solution active with dislocation creep in quartz. Field of view is 3.3 mm. (d) Synkinematic growth of muscovite within micro pull-aparts of Mesozoic kyanite. Field of view is 3.3 mm.

oriented normal to the fractures [see also *Malavieille*, 1987, Figure 11b] suggestive of fibrous growth and solution mass transfer and precipitation [e.g., *Etheridge et al.*, 1984]. The lack of preserved microstructures indicative of dynamic recrystallization in potassium feldspar implies that no shearing took place at temperatures higher than ~450°C [*FitzGerald and Stunitz*, 1993]. These microstructures collectively indicate that a significant component of deformation occurred at temperatures of 300-400°C [*Simpson and Depaor*, 1993; *Passchier and Trouw*, 1996]. Temperatures during the late stages of plastic deformation were probably no greater than ~350°C, and possibly as low as 275°C, as hydrolytic weakening of quartz lowers the minimum temperatures required for quartz plasticity [e.g., *Koch et al.*, 1989; *Kronenberg*, 1994].

Petrographic observations of the Elba Quartzite indicate two phases of muscovite growth. Muscovite and kyanite occur as porphyroclasts within the schistose parts of the quartzite mylonite and are interpreted as relicts of the prograde Mesozoic metamorphic assemblage. Early grown muscovite grains have been dismembered and strung out along shear foliations (*c* surfaces and shear bands) by a variety of mechanical processes [e.g., *Lister and Snoke*, 1984]. Younger muscovite occurs within the necks of pulled apart kyanite porphyroclasts and is parallel to the principal finite stretch direction, documenting growth of muscovite during shearing (Figure 5d).

3. The $^{40}Ar/^{39}Ar$ and Fission Track Thermochronology Results

Archean and Proterozoic rocks from the footwall of Raft River detachment were collected for thermochronology at localities spaced 4 to 5 km apart, along a 25-km-long transect parallel to the hanging wall transport direction (Figures 2 and 3). This transect was extended farther west for an additional 22 km for collection of apatite for fission track analysis (Figure 1).

To permit time-temperature histories to be constructed, several approaches were taken to define the thermal significance of the $^{40}Ar/^{39}Ar$ apparent ages. First, closure temperature estimates were used from previous empirical field studies and from previous integration of the experimentally determined kinetic parameters for diffusion, with permissive cooling rates. These estimates permit a range in closure temperatures for

biotite (280-350°C), muscovite (325-400°C), and hornblende (550-450°C) [*Snee et al*, 1988; *Hames and Bowring*, 1994; *Harrison et al.*, 1985; *Lister and Baldwin*, 1996; *McDougall and Harrison*, 1999] that were used in constructing cooling curves. Second, forward modeling of the muscovite and biotite age spectra was done using the MacArgon program, version 5.0, described by *Lister and Baldwin* [1996]. The MacArgon program models the distribution of argon within the crystal lattice when subjected to an arbitrary P-T-t path. The cooling curves determined in the first approach above were used as a starting point for the modeling with MacArgon.

The analyses of the K-feldspar concentrates were treated differently, following the multiple diffusion domain approach of *Lovera et al.* [1989, 1991]. The recognition that K-feldspar has a distribution of discrete diffusion domains implies that each diffusion domain has a distinct closure temperature. This allows a segment of the cooling history to be reconstructed from an individual mineral analysis. In this study, a single activation energy was assumed to best represent all diffusion domains for each K-feldspar and was determined by a linear regression of the lower-temperature steps of the experiment on an Arrhenius diagram [*Lovera et al.*, 1989]. The frequency factor for each diffusion domain was determined by using the determined activation energy and modeling the form of the Arrhenius plot using the software of *Lovera* [1992]. The number of diffusion domains and their volume fractions were modeled by using an iterative technique to determine the best fit between experimental and modeled results on a log of relative domain size [$\log(r/r_0)$] versus cumulative percent ^{39}Ar released plot. Using the calculated diffusion parameters and domain size distribution, the thermal histories were determined by iterative best fitting of the synthetic to the measured apparent age spectra.

Apatite and zircon fission track ages and apatite confined track length measurements were used to define the low-temperature portions of the cooling histories. The temperature significance of the apatite fission track ages was conservatively interpreted as 110-60°C (the partial annealing zone, [*Gleadow and Fitzgerald*, 1987; *Fitzgerald and Gleadow*, 1988]). However, the closure temperature is a function of cooling rate, and for moderate to rapid cooling rates (for example in excess of 12°C/m.y.) apatite fission track ages can be considered to represent the time of cooling through a closure temperature of ~110°C. Apatite fission track length measurements were used to constrain the rate and path of cooling of a sample within the partial annealing zone [e.g., *Gleadow et al.*, 1986]. Monte Trax, a track-length modeling program [*Gallagher*, 1995], was used to constrain the thermal histories for two samples. The behavior of fission tracks in zircon is not as well-constrained as in apatite; a recent field study suggests that the zircon fission track partial annealing zone ranges from 230 to 330°C [*Tagami and Shimada*, 1996]. *Foster et al.* [1996] obtained estimates of the zircon fission track closure temperature of ~260-240°C by comparing $^{40}Ar/^{39}Ar$ K-feldspar analyses with zircon fission track analyses of several Basin and Range samples. The results from this study are consistent with those of *Foster et al.* [1996], and therefore the data are discussed in terms of a closure temperature of ~250 ± 10°C.

Below we report results of $^{40}Ar/^{39}Ar$ and fission track analyses for 35 mineral concentrates. Sample locations are shown in Figure 2. The $^{40}Ar/^{39}Ar$ data tables and a description of the analytical methods are available as an electronic supplement[1]. Results are presented in Figures 6-11 and Tables 1-3. We first discuss the general results and spatial cooling age trends by mineral phase and then discuss individual samples in consideration of construction of cooling curves for each sample locality.

3.1. Hornblende

Six hornblende samples were analyzed by the $^{40}Ar/^{39}Ar$ method. All hornblende samples are from Archean amphibolite beneath the base of the shear zone, with the exception of RR91-42 (Dunn Creek), which is from a hornblende-bearing quartzite within the base of the shear zone. Hornblende from all sample localities yields discordant, generally saddle-shaped age spectra interpreted to result from varying degrees of incorporation of excess argon [*Harrison and McDougall*, 1981] (Figure 6). The age minima show no systematic relationship with location and range from 90 to 55 Ma. No single gas fraction in all six hornblende analyses, each with 17 or more heating steps, is younger than 55 Ma. Analysis of the hornblende data on $^{36}Ar/^{40}Ar$ versus $^{39}Ar/^{40}Ar$ isotope correlation diagrams did not resolve the degree of contamination by excess argon and did not clarify the appropriate cooling ages. The conservative interpretation of the hornblende data is that the age spectra minima represent maximum ages for hornblende cooling. A further constraint is provided by the inferred temperature conditions of shearing within the Raft River shear zone. Microstructural observations of quartz and feldspar, mentioned previously, indicate relatively low-temperature (300 - 400°C) deformation conditions and a notable lack of earlier higher-temperature deformation associated with the top-to-the-east shearing fabric. This observation, together with the minimum ages that range from 55 to 90 Ma, suggests that the footwall to the Raft River detachment had cooled to temperatures below closure for metamorphic hornblende prior to the onset of top-to-the-east shearing, during the latest Mesozoic to early Tertiary.

3.2. Muscovite

Seven muscovite concentrates were extracted, six from the lower 15 m of the Proterozoic Elba Quartzite and one (RR91-48) from near the top of the unit (Figure 2). All samples of the Elba Quartzite exhibit variable development of mylonitic fabric, with intensity of fabric increasing toward the east.

The muscovite age spectra are characterized by varying degrees of discordancy, and the degree of discordancy decreases to the east with decreasing apparent age. The muscovite age spectra generally exhibit steep age gradients over the first 20% of ^{39}Ar released, flattish segments from 20 to 80% ^{39}Ar released, and age gradients in the highest-temperature gas fractions from ~80 to 100% ^{39}Ar released (Figure 7a). The flattish portions from 20 to 80% ^{39}Ar released are interpreted to record cooling through the effective closure temperature (see discussion below). Plateau ages and preferred ages were calculated for these portions of the age spectra (Table 1).

The muscovite apparent ages yield a spatial age gradient with younger apparent ages toward the east, in the downdip

[1]Supporting data tables and analytical methods are available on diskette or via Anonymous FTP from kosmos agu.org, directory APEND (Username = anonymous, Password = guest). Diskette may be ordered from American Geophysical Union, 2000 Florida Avenue, N.W., Washington, DC 20009 or by phone at 800-966-2481, $15.00. Payment must accompany order.

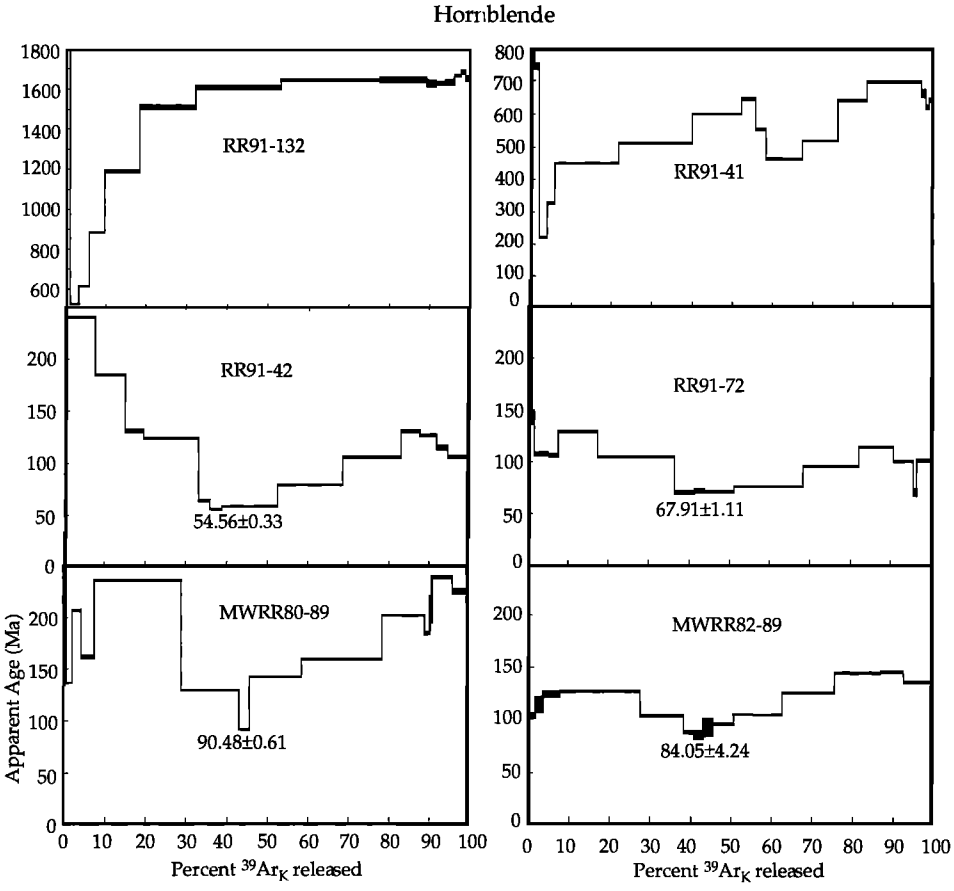

Figure 6. The $^{40}Ar/^{39}Ar$ apparent age spectra of hornblende from Archean amphibolite of the Raft River Mountains. Note that all samples are significantly affected by excess argon. Numbers on age spectra indicate ages of minima.

and hanging wall transport direction of the shear zone and detachment fault. From west to east, the muscovite total gas ages decrease from 46.6 to 14.7 Ma (Figure 7a). Total gas ages become abruptly younger by about 23 m.y. between the Pine and Fisher Creek Canyon localities, over a lateral distance of 4.4 km.

3.3. Biotite

Biotite age spectra, similar to muscovite, yield discordant age spectra with younger apparent ages toward the east. From west to east, the gradients in biotite total gas ages are 44.0 to 13.4 Ma (Figure 7b). Biotite cooling ages become abruptly younger by 24 m.y. between the Century Hollow and Fisher Creek Canyon localities, over a lateral distance of 11.4 km. The morphologies of the biotite age spectra are less discordant than coexiting muscovite and are characterized by slight age gradients in the highest-temperature gas fractions, flattish segments from 20 to 80% ^{39}Ar released, and steep age gradients for the first 20% of ^{39}Ar released (Figure 7b). Similar to the interpretation for muscovite, the flattish portions from 20 to 80% ^{39}Ar gas released are interpreted as recording cooling through the effective closure temperature. Plateau ages and preferred ages were calculated for these portions of the age spectra (Table 1).

3.4. K-feldspar

Six K-feldspar separates were prepared and analyzed (Figure 8). Samples from Big Hollow, Pine Creek, Fisher Creek, Dunn Creek, and Indian Creek Canyons are from undeformed to weakly deformed Archean adamellite beneath the base of the shear zone, 60 to 180 m beneath the base of the Elba Quartzite. The Ten Mile Canyon sample was collected from the Elba Quartzite, 15 m above the base of the unit. The initial K-feldspar analyses were conducted before isothermal duplicate heating steps were routinely employed to resolve excess argon associated with lattice and surface sites that degas early in a temperature step [*Harrison et al.*, 1994]. The samples least affected by excess argon (RR-91-17, RR91-96; Figures 8 and 9) were reanalyzed using duplicate isothermal steps to better determine the age and diffusion parameters. The modeled Arrhenius, log of relative domain size [$\log(r/r_0)$] versus cumulative percent ^{39}Ar released, and age spectrum plots are shown only for these two samples (Figure 9). The diffusion parameters determined for all samples are shown in Table 2.

The six K-feldspar age spectra are generally saddle-shaped, interpreted to result from varying degrees of incorporation of excess argon (Figure 9). Sample RR91-17 (Pine Creek) is the least affected by excess argon and yields ages from large diffusion domains intermediate between biotite and muscovite ages (Figure 8). The calculated closure temperature for the large diffusion domain is 345°C, compatible with a temperature intermediate between muscovite and biotite closure (Table 2). Sample RR91-96 from Dunn Creek yields ages from large diffusion domains older than coexisting muscovite; however, calculated closure temperature for the largest domain is 384°, permissibly more retentive than muscovite. The other four samples yield ages for large diffusion domains

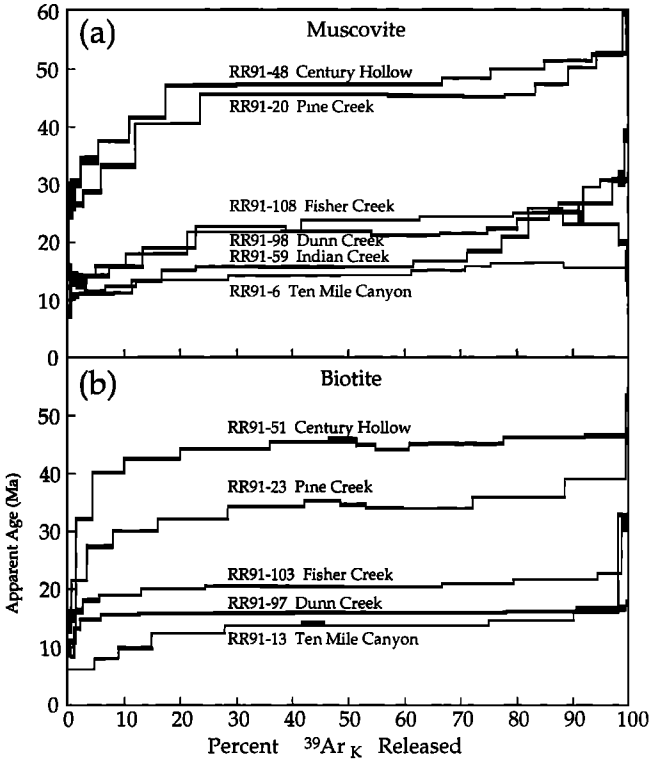

Figure 7. (a) The $^{40}Ar/^{39}Ar$ apparent age spectra of muscovite from the Elba Quartzite of the Raft River Mountains. Note spatial age gradient, with apparent ages becoming younger toward the east, and steep gradient in apparent ages between the Pine and Fisher Creek locations. Only coarsest of two analyzed size fractions from Pine Creek shown for clarity. (b) The $^{40}Ar/^{39}Ar$ apparent age spectra of biotite from the Raft River Mountains. Samples RR91-23, -103, -97 and -13 are from the Archean older schist; sample RR91-51 is from the Proterozoic schist of Upper Narrows.

significantly older than coexisting muscovite. For these later samples, only the flattish to shallow age gradients were modeled using the multidomainal approach of *Lovera et al.* [1991], and these cooling path segments were treated as providing a maximum age to the cooling path.

3.5. Zircon

Eight concentrates of zircon were extracted from the Archean adamellite and the Elba Quartzite. Only three concentrates were analyzed due to the metamict character of many of the samples. Zircon fission track ages are tabulated in Table 3.

3.6. Apatite

Seven samples of apatite were analyzed, track lengths were measured on four, and two of these were modeled using the track length modeling program Monte Trax [*Gallagher*, 1995] (Figure 10). Apatite fission track ages range from 10.8 Ma in Century Hollow (west end of main transect) to 7.4 Ma in Indian Creek Canyon (east end) and ages are consistently younger to the east (Table 3). Sample elevations ranged from 2037 to 2720 m, and the ages show no correlation with elevation. The sampled transect was extended farther west for apatite analyses to the northern Grouse Creek Mountains and includes localities at Clarks Basin (sample location 7 in Figure 1, 11.2 Ma) and on the crest of the northern Grouse Creek Mountains at the headwaters to Kimbell Creek (sample location 8 in Figure 1, 13.5 Ma).

4. Construction and Interpretation of Cooling Histories

The $^{40}Ar/^{39}Ar$ thermochronological data for muscovite, biotite, K-feldspar, and hornblende and the apatite and zircon fission track data are combined to construct cooling curves or cooling path envelopes [after *Dokka et al.*, 1986] for footwall sample localities beneath the Raft River detachment (Figure 2). In constructing the cooling path envelopes we assume a linear extrapolation of temperature between defined cooling ages. The following temperature ranges were used in their conservative construction: 325-400°C, muscovite; 280-350°C, biotite; 240-260°C, zircon; and 110-60°C, apatite. K-feldspar analyses were modeled using the methods of *Lovera et al.* [1989, 1991] and best fit thermal models are shown within the permissive cooling path envelopes (Figure 11). Also shown are best fit thermal models from MacArgon modeling of coexisting muscovite and biotite age spectra. The potential complication of post argon closure shearing between samples was minimized by sampling beneath and within the basal portion of the shear zone. Because the lowest-temperature thermochronometers come from the structurally deeper levels beneath the shear zone, restoration of any post-argon-closure shear that may have occurred between samples would have the effect of decreasing the cooling age of the mineral at that locality, effectively increasing the cooling rate.

4.1. Century Hollow

Century Hollow is the westernmost sampling locality within the Raft River detachment footwall. At this location the quartzite of Yost, stratigraphically higher than the schist of Upper Narrows, is present in the footwall of the Raft River detachment, indicating that the detachment fault cuts slightly down section to the east. The Elba Quartzite displays evidence for mild intracrystalline plasticity related to top-to-the-east shearing, and at microscopic scale, quartz shows a preferred orientation of deformation bands indicating development of prismatic subgrain boundaries that dip moderately to the west with respect to foliation and small amounts of intracrystalline strain. A quartz lattice-preferred orientation study shows maxima consistent with dominantly subbasal slip in <*a*>, consistent with low-temperature plasticity in quartz (Figure 4a). Muscovite (RR91-48) yields a total gas age of 46.63 ± 0.21 Ma (preferred age, 47.35 ± 0.14 Ma), and the low-temperature increments define an apparent argon loss pattern with an intercept of about 26-30 Ma (Figure 7a and Table 1). Biotite (RR91-51) yields a total gas age of 44.01 ± 0.16 Ma (preferred age, 45.38 ± 0.36 Ma) (Figure 7b and Table 1). Apatite fission track analysis yields an age of 10.8 ± 0.9 Ma, with a mean track length of 14.2 ± 0.1 μm (Table 3). The cooling history indicates moderate to rapid cooling (~25°C/m.y.) in the late Eocene as recorded by a 2.0-m.y. difference in the muscovite and biotite $^{40}Ar/^{39}Ar$ preferred ages (Figure 11a). Track length modeling of fission tracks in apatite indicates a cooling rate in the late Miocene of 60°C/m.y. through the apatite partial annealing zone (Figure 10, bottom).

Table 1. The $^{40}Ar/^{39}Ar$ Age Spectra Results for Muscovite and Biotite

Sample	Location	Rock Unit	Mineral	Total Gas Age, Ma	Preferred Age, Ma	Steps	Grain Size Analyzed, μm
RR91-48	CH [6]	Pe	muscovite	46.63 ± 0.21	47 35 ± 0.14	8-11 (49.3%)	88-105
RR91-51	CH [6]	Pun	biotite	44 01 ± 0.16	45.38 ± 0.36	5-11 (72.6%)	125-150
RR91-20	PC [5]	Pe	muscovite	43 75 ± 0.21	45.16 ± 0.29	8-12 (59.8%)	88-105
RR91-20	PC [5]	Pe	muscovite	43.94 ± 0 08			74-88
RR91-23	PC [5]	Aos	biotite	33.69 ± 0.11			125-150
RR91-108	FC [4]	Pe	muscovite	22.45 ± 0.13			125-150
RR91-103	FC [4]	Aos	biotite	20.29 ± 0.12	20.24 ± 0 17	5-10 (66.4%)	125-150
RR91-98	DC [3]	Pe	muscovite	21 48 ± 0.20	21.90 ± 0.37	8-12 (57.6%)	125-150
RR91-97	DC [3]	Aos	biotite	16.20 ± 0.06	15.91 ± 0.09	5-11 (72.4%)	125-150
RR91-59	IC [2]	Pe	muscovite	16.91 ± 0.11			125-50
RR91-6	TM [1]	Pe	muscovite	14.66 ± 0.09	15.05 ± 0.18	5-13 (75.7%)	88-105
RR91-7	TM [1]	Pe	muscovite	14.57 ± 0.10	14.88 ± 0.17	8-12 (68.7%)	125- 50
RR91-13	TM [1]	Aos	biotite	13.44 ± 0.06	13.89 ± 0.27	4-11 (74.1%)	125-150

Preferred ages were calculated by taking a weighted mean over the "flattish" portion of the age spectra. Locality abbreviations: CH, Century Hollow, DC, Dunn Creek, FC, Fisher Creek, IC, Indian Creek, TM, Ten Mile Canyon, PC, Pine Creek. Brackets following location abbreviations indicate localities on Figure 1. Rock unit abbreviations: Pe, Proterozoic Elba Quartzite; Pun, Proterozoic schist of Upper Narrows; Aos, Archean older schist.

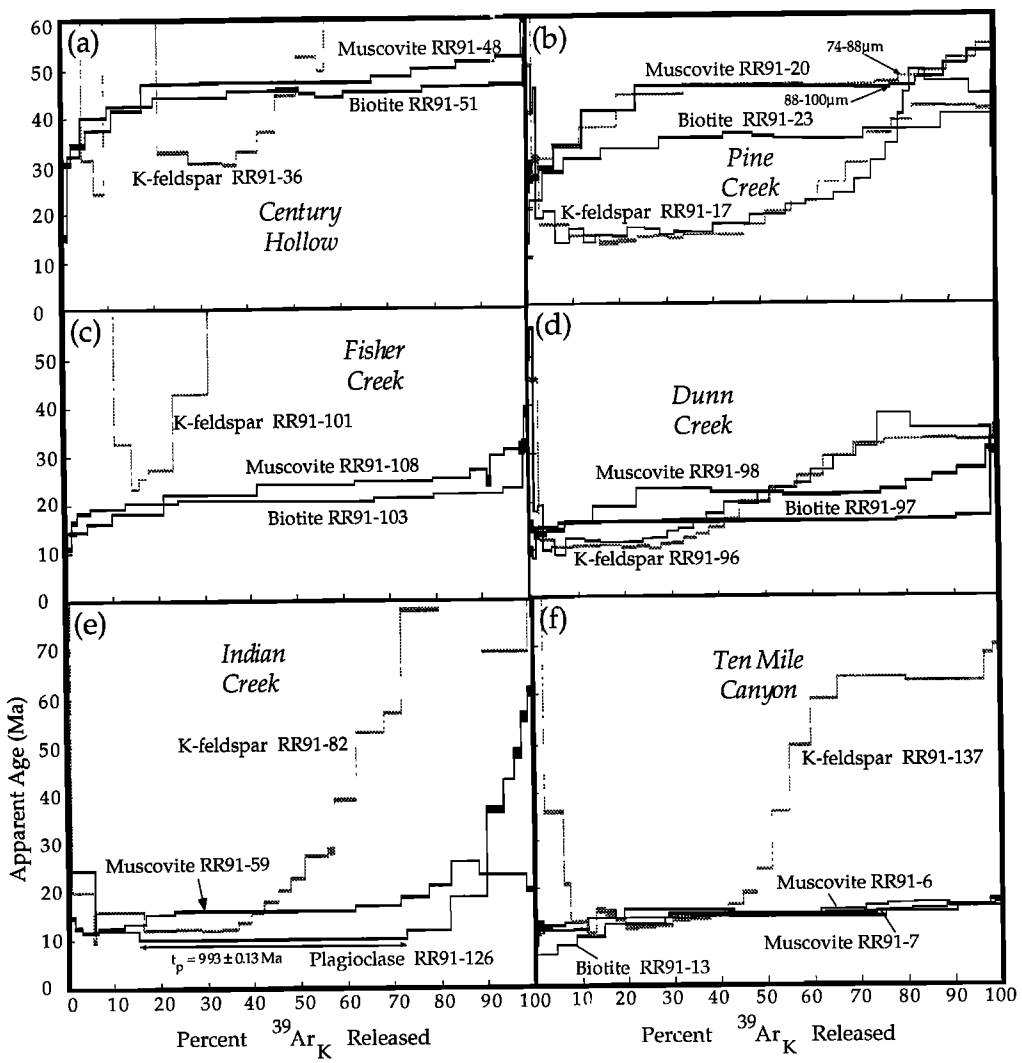

Figure 8. The $^{40}Ar/^{39}Ar$ apparent age spectra of muscovite, biotite, K-feldspar, and plagioclase from the Raft River Mountains. Two analyses with different heating schedules are shown for K-feldspar samples RR91-17 (Pine Creek) and RR91-96 (Dunn Creek), the second (black fill) has isothermal duplicate heating steps at low experimental temperatures.

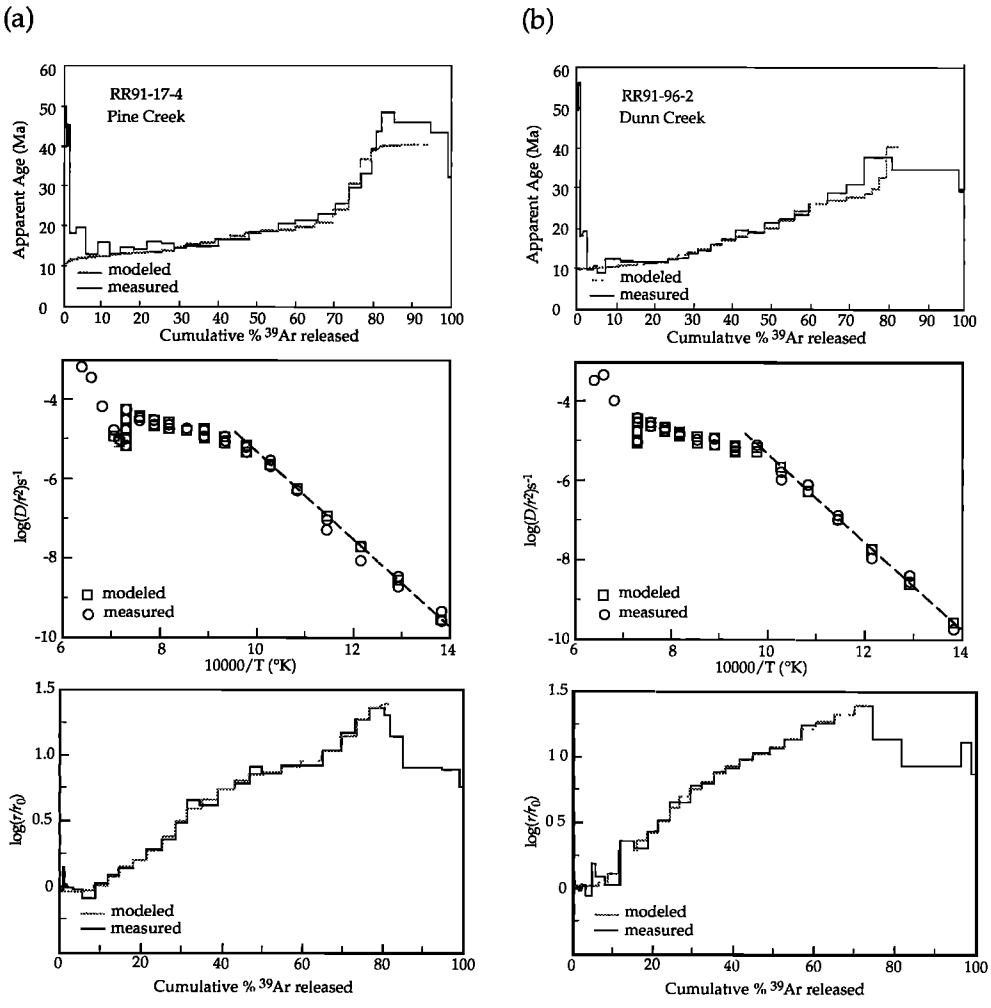

Figure 9. K-feldspar models. (a) RR91-17. Modeling the release of ^{39}Ar over the first 11 heating increments indicates an activation energy [E] of 50.09 kcal/mol and a log frequency factor/effective domain size parameter [$\log(D_0/r_0^2)$] of 5.55 s^{-1}. Modeling the domain size distribution on a plot of log of relative domain size [$\log(r/r_0)$] versus cumulative percent ^{39}Ar released indicates a reasonable fit using six diffusion domains whose closure temperatures range from 222 to 346°C (Table 2). (b) RR91-96. Modeling of release of ^{39}Ar over the first isothermal heating steps of the first seven heating increments indicates an activation energy [E] of 51.22 kcal/mol and a log frequency factor/effective domain size parameter [$\log(D_0/r_0^2)$] of 5.90 s^{-1}. Modeling the domain size distribution indicates a reasonable fit using eight diffusion domains whose closure temperatures range from 225 to 384°C (Table 2).

4.2. Pine Creek

Muscovite (RR91-20) from Pine Creek yields a total gas age of 43.75 ± 0.21 Ma and a preferred age of 45.16 ± 0.29 Ma (Figure 7a and Table 1). Biotite (RR91-23) yields a discordant age spectra with a total gas age of 33.69 ± 0.11 Ma (Figure 7b and Table 1). K-feldspar (RR91-17) yields a saddle-shaped age spectrum that exhibits significant excess argon in the first 5% of gas released and rises monotonically from 12.98 to 48.46 Ma (Figure 7b). Synthetic age spectra that provide a best fit to the measured age spectra (Figure 9a), using the calculated diffusion parameters and domain size distribution (Table 2), indicate rapid cooling from ~320°C at 16 Ma through 220°C at 11 Ma. Zircon fission track yields an age of 10.8 ± 0.8 Ma (Table 3). Apatite fission track analysis yields an age of 8.6 ± 0.6 Ma and a mean track length of 14.0 ± 0.1 μm (Table 3). The cooling history indicates moderately rapid cooling to 300°C between 47 and 44 Ma, followed by relatively constant temperature with possible very slow cooling throughout the Oligocene and early Miocene (Figure 11b). Rapid cooling begins at about 16 Ma and continues through apatite closure at 8.6 Ma. Cooling rates constrained by K-feldspar modeling and zircon and apatite fission track are ~28 to 40°C/m.y. overall and increase from ~20°C/m.y. (16 to 11 Ma) to >66°C/m.y. (11 to 8.6 Ma). Track length modeling of fission tracks in apatite indicates cooling rates through the partial annealing zone in excess of 100°C/m.y. (Figure 10).

4.3. Fisher Creek

Muscovite (RR91-108) yields a total gas age of 22.45 ± 0.13 Ma, and biotite (RR91-103) yields a total gas age of 20.29 ± 0.12 Ma (preferred age 20.24 ± 0.17 Ma) (Figure 7 and Table 1). K-feldspar (RR91-101) exhibits a saddle-shaped age spectra with a minimum age of 23 Ma (Figure 8c), older than

Table 2. Kinetic Parameters for K-feldspar Diffusion Models

Diffusion Parameters	RR91-17	RR91-96	RR91-82	RR91-137
E, kcal/mol	50.09	51.22	51.22	51.67
$\log(D/r_1)$	7.399	7.748	7.114	8.989
ρ_1	0.0681	0.0757	0.1976	0.0515
Tc_1	222°	225°	238°	204°
$\log(D/r_2)$	6.388	6.513	6.3812	7.451
ρ_2	0.0343	0.1046	0.0996	0.0514
Tc_2	244°	253°	256°	236°
$\log(D/r_3)$	6.356	5.5867	4 0142	6.0876
ρ_3	0.1144	0 0714	0 7027	0.0319
Tc_3	245°	276°	320°	268°
$\log(D/r_4)$	5.3576	4.652		5.370
ρ_4	0.0816	0.1759		0.1855
Tc_4	270°	301°		286°
$\log(D/r_5)$	4.1746	3.732		3.603
ρ_5	0.3609	0.1525		0.6796
Tc_5	302°	328°		337°
$\log(D/r_6)$	2.749	3.674		
ρ_6	0.3406	0.1750		
Tc_6	346°	339°		
$\log(D/r_7)$		2.065		
ρ_7		0.245		
Tc_7		384°		

ρ is the volume fraction of each domain

coexisting muscovite and biotite, and all gas increments are interpreted to be affected by excess radiogenic argon. Apatite fission track analysis yields an age of 8.1 ± 0.9 Ma (Table 3).

4.4. Dunn Creek

Muscovite (RR91-98) from Dunn Creek Canyon yields a total gas age of 21.48 ± 0.2 Ma (preferred age, 21.90 ± 0.37 Ma), and biotite (RR91-97) yields a total gas age of 16.20 ± 0.06 Ma (preferred age, 15.91 ± 0.09 Ma) (Figure 7 and Table 1). K-feldspar (RR91-96) yields a saddle-shaped age spectrum that exhibits significant excess argon in the first 5% of gas released and rises monotonically from 10.01 to 37.96 Ma (Figure 8). Synthetic age spectra that provide a best fit to the measured age spectra, using the calculated diffusion parameters and domain size distribution (Table 2), indicate moderate cooling from about 325°C at 16 Ma to 290°C at 10.5 Ma, followed by rapid cooling through 225°C at 10-9 Ma (Figures 9b and 11d). Zircon fission tracks yield a seemingly anomalously old age of 13.4 ± 1.8 Ma (Table 3) and may indicate a closure temperature higher than that adopted here, although it is compatible within 2σ analytical error with K-feldspar small domain ages corresponding to ~250°C (Figure 11d). Because of this uncertainty in closure temperature, the zircon analysis is discounted in favor of the K-feldspar and mica modeling results in construction of the cooling path envelope. Apatite fission track analysis yields an age of 7.6 ± 1.3 Ma (Table 3). The constructed cooling curve shows cooling rates increasing throughout the Miocene, with final cooling rates of about 85°C/m.y (Figure 11d).

Table 3. Fission Track Analytical Results for Apatite and Zircon

Sample	Locality	Rock Unit	Number of Grains	Standard Track Density, $x10^6$ cm^{-2}	Fossil Track Density, $x10^4$ cm^{-2}	Induced Track Density, $x10^4$ cm^{-2}	Uranium, ppm	Chi-square Probability %	Fission Track Age, Ma ± 1σ	Mean Track Length, μm	Std. Dev., μm
					Apatite						
RR91-17	PC [5]	Aad	20	2.00 (3198)	14.7 (199)	550.7 (7446)	26	75	8.6 ± 0.6	14.0 ± 0.1 (105)	1.06
RR91-82	IC [2]	Aad	15	2.24 (3576)	7.6 (57)	364.8 (2754)	17	93	7.4 ± 1.0		
RR91-96	DC [3]	Aad	20	2.22 (3544)	3.5 (33)	161.9 (1535)	8	97	7.6 ± 1.3		
RR91-101	FC [4]	Aad	20	2.24 (3576)	8.0 (90)	353.2 (3977)	17	59	8.1 ± 0.9		
RR91-175	CH [6]	Aad	20	2.00 (3198)	11.6 (144)	342.6 (4272)	16	10	10.8 ± 0.9	14 2 ± 0.1 (101)	1.22
RR92-12	CB [7]	Aad	20	2.06 (3304)	7.58 (97)	222.42 (2847)	11	23	11.2 ± 1.2	14.0 ± 0.3 (10)	1.09
GC-39	KC [8]	Pe	20	2 08 (3340)	21.7 (146)	538.69 (3620)	26	8	13.5 ± 1.1	14.9 ± 0.2 (48)	1.15
					Zircon						
RR91-6	TMC [1]	Pe	11	0.18 (1167)	79.9 (218)	260.4 (711)	125	81	9.4 ± 0.7		
RR91-20	PC [5]	Pe	9	0.18 (1167)	89 6 (224)	254.4 (636)	120	92	10.8 ± 0.8		
RR91-98	DC [3]	Pe	8	0.18 (1155)	54.2 (77)	122.5 (174)	58	66	13.4 ± 1.8		

Parentheses show number of tracks counted. Standard and induced track densities were measured on mica external detectors (geometry factor = 0.5), and fossil track densities were measured on internal mineral surfaces. Ages were calculated using the standard fission track age equation [e.g., *Hurford and Green*, 1983]. Samples irradiated in the Cornell University Triga reactor. Zeta is 320 ± 9 (apatite) and 335 ± 20 (zircon) for A. E. Blythe for dosimeter glass SRM 962. CB, Clarks Basin, CH, Century Hollow, DC, Dunn Creek, FC, Fisher Creek, IC, Indian Creek, KC, Kimbell Creek, TM, Ten Mile Canyon, PC, Pine Creek; numbers following locality abbreviations in brackets refer to localities on Figure 1. Rock unit abbreviations: Pe, Proterozoic Elba Quartzite; Aad, Archean adamellite.

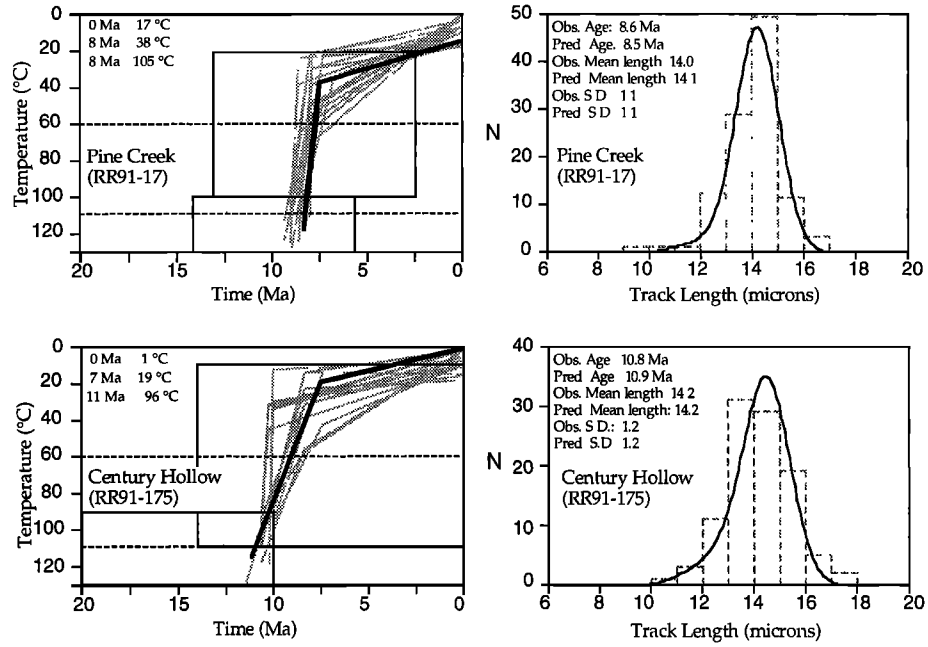

Figure 10. Modeled thermal histories and fission track length distributions for apatite samples (top) RR-91-17 and (bottom) RR-91-175. The *Laslett et al.* [1987] Durango apatite annealing model and an initial mean track length of 15.0 μm were specified in the modeling, as were time-temperature boundaries for three points. The boundaries of two of these points are represented by the boxes within each model figure; the third constraint was the modern mean annual temperature (10 ± 10°C). The straight dashed lines represent the bounds of the partial annealing zone at 60 and 110°C. The genetic algorithm approach [see *Gallagher*, 1995] was used in the track length modeling, with 50 thermal histories generated during each of 10 iterations. The lighter gray lines on the time-temperature plots represent the possible solutions generated in the 10th iteration; the black line is the "best fit" solution for each sample (with the times and temperatures for three points on the best fit solution listed to the left within the plot). The gray dashed lines on the histogram plots (to the right) are the observed (measured) track length distributions for each sample; the solid curve is the predicted track length distribution for the best fit thermal history. The observed and predicted age, mean track lengths, and standard deviations are listed for comparison.

4.5. Indian Creek

Muscovite (RR91-59) yields a total gas age of 16.91 ± 0.11 Ma (Figure 7a and Table 1). In contrast, biotite yields a total gas age of 24.59 ± 0.2 Ma. The biotite is from retrogressed amphibolite containing both hornblende and biotite, whereas all other biotite separates are from samples of the psammatic older schist that lacked hornblende. This biotite analysis clearly records incorporation of excess radiogenic argon. Apatite fission track analysis yields an age of 7.4 ± 1.0 Ma (Table 3).

A diabase sill locally intrudes along and parallel to the Raft River detachment in two localities at the head of Indian Creek Canyon [*Compton*, 1975]. Although this unit is only exposed as subcrop at best, float and subcrop of this unit can be mapped continuously around two klippen of Ordovician rocks, indicating its sheet-like intrusive nature along the detachment fault [*Compton*, 1975]. The diabase exhibits no crystal-plastic deformation features and, aside from few epidote- and chlorite-filled fractures, is relatively undeformed. Although the exposure does not allow the exclusion of the possibility that the sill is boudinaged rather than penetratively deformed, the very minor internal deformation of the rock is most compatible with its being emplaced after distributed ductile shearing had ended and deformation had localized to the overlying brittle fault zone.

A plagioclase separate from this sill yields a disturbed saddle-shaped age spectrum interpreted to record excess argon at both high and low experimental temperatures (Figure 8e). The intermediate temperature portion (800 to 1000°C) of the release spectra, however, is interpreted to be unaffected by excess argon and yield an age representative of crystallization. Three gas increments comprising over 57% of ^{39}Ar released yield a plateau age of 9.93 ± 0.13 Ma, as compared to a total gas age of 15.20 ± 0.16 Ma.

4.6. Ten Mile Canyon

Ten Mile Canyon is the easternmost sample locality and represents the structurally deepest exposed level of the Raft River detachment fault footwall. Rocks in this area record the highest strain of all sampled localities. Two samples of muscovite were analyzed, sample RR91-6 from quartzite mylonite and sample RR91-7 from quartz-muscovite-kyanite schist, 1.2 km farther west. RR91-6 yields a total gas age of 14.66 ± 0.09 Ma (preferred age, 15.05 ± 0.18 Ma), and sample RR91-7 yields a total gas age of 14.57 ± 0.10 Ma (preferred age 14.88 ± 0.17); both muscovite analyses are consistent within 1σ analytical error (Figure 8f). Both analyses exhibit lower-temperature intercepts of about 8-10 Ma. Biotite (RR91-13) yields a total gas age of 13.44 ± 0.06 Ma (preferred age, 13.89 ± 0.27 Ma) (Figure 7b and Table 1). This biotite, in contrast to other concentrates analyzed, contains petrographically distinct retrograde chlorite, which may be responsible for the younger apparent ages in the low-temperature steps. Zircon fission track analysis yields an age of 9.4 ± 0.7 Ma (Table 3).

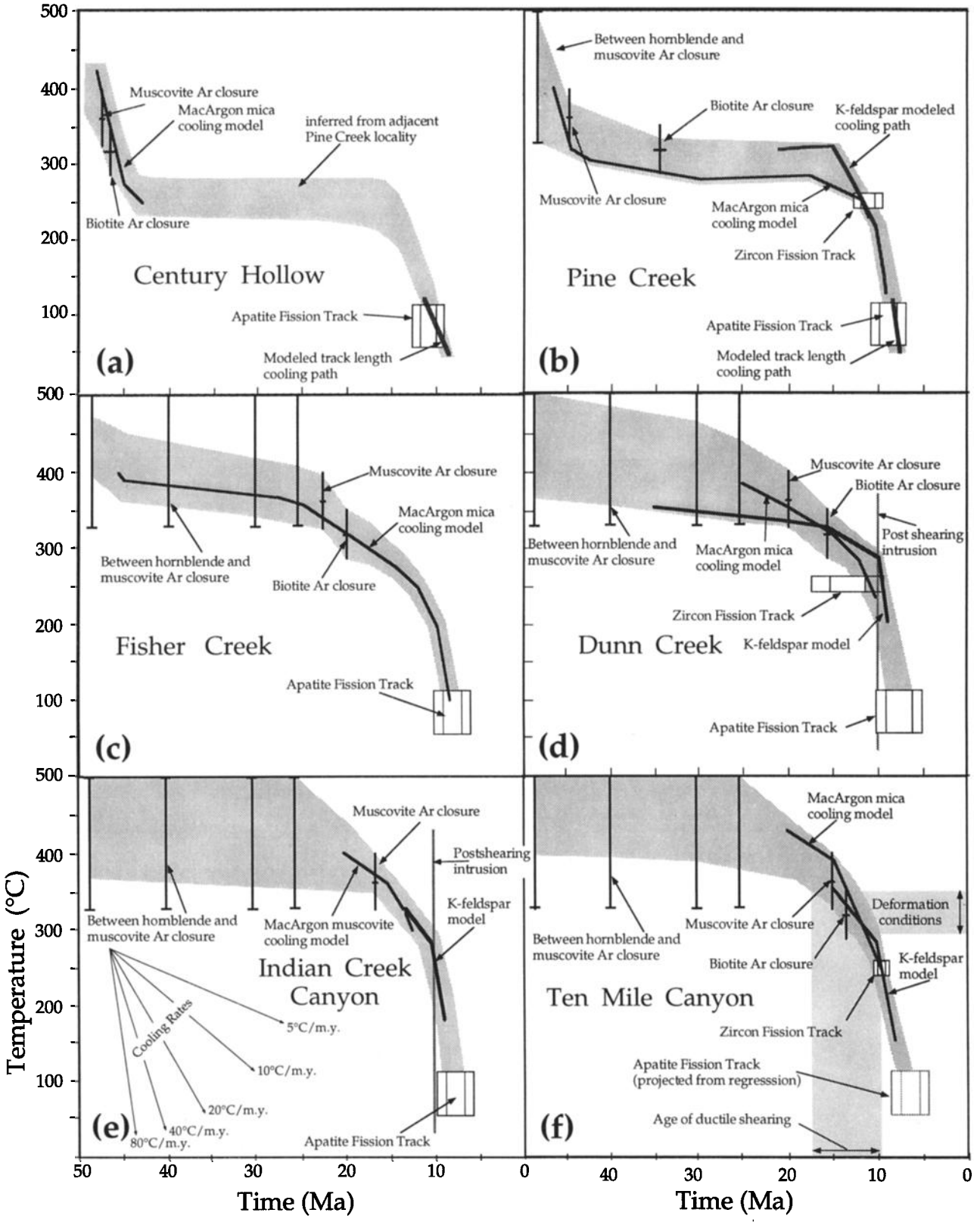

Figure 11. Cooling curves for sampled localities. (a) Century Hollow; (b) Pine Creek; (c) Fisher Creek; (d) Dunn Creek; (e) Indian Creek; (f) Ten Mile Canyon. Apatite RR91-82 is from an intermediate position between Ten Mile and Indian Creek localities. The vertical bars are conservative permissible temperatures for the basement unconformity, based on hornblende, muscovite, and biotite cooling ages and K-feldspar multidiffusion domain analysis. Double boxes are apatite and zircon fission track analyses at 1 and 2 sigma. Shaded box is an interpolated age for this locality, based on regression of Figure 16. The shaded area is the permissible cooling path envelope.

5. Interpretation of Mica Intrasample and Intersample Age Gradients

Intrasample age gradients of micas can result from a variety of mechanisms, including mixing of two or more compositionally distinct mica populations, selective recrystallization and growth of new mica, cooling of mica with a distribution of grain size, slow cooling through the closure interval for argon diffusion, enhanced diffusion of radiogenic argon during shearing, reheating, or by a combination of these mechanisms. Intersample cooling age variations can result from the above mechanisms, as well as from differential cooling along variable T-t paths. In sections 5.1. to 5.4. we examine the possible explanations for the intrasample and intersample age gradients.

5.1. Grain Size

The mechanical fragmentation of mica fish [e.g., *Lister and Snoke*, 1984] during greenschist facies shearing produces a reduction in grain size and, because of the heterogeneous nature of this process, a distribution of grain sizes. Other processes, such as unequal nucleation and growth, can also lead to a distribution in grain size. If the diffusion radius of argon in micas is a function of the grain size radius [*Hames and Bowring*, 1994], the effective closure temperatures will vary with grain size, and a distribution in grain size can result in mica grains with varying argon retentivity [*Goodwin and Renne*, 1991]. Furthermore, cooling of a mica population with a distribution in grain size can produce an apparent argon loss gradient whose steepness is inversely proportional to cooling rate. This potential effect is difficult to test in the quartzite and schist samples because the mechanical fragmentation of grains during the rock crushing process cannot be avoided, and the analyzed grain size and grain size distribution of the mineral separates do not reflect the grain size and grain size distribution within the rock as it cooled [*Goodwin and Renne*, 1991]. To further investigate the potential effect of grain size, two different grain size fractions were analyzed in sample RR91-20 (Pine Creek), which exhibited the largest apparent argon loss pattern. The grain size in this sample is fairly restricted, however, so the differences in grain size between fractions analyzed are not large. Nonetheless, both fractions yield very similar age spectra morphology and ages (Figure 8b), suggesting that the intrasample age gradients are not due to a distribution in grain size. However, if the grains occur as clusters, the effective grain size can be smaller than the analyzed grain size, and the effect of a distribution in effective grain sizes could be important.

There is an overall increase in the average natural grain size within the quartzite and quartz-muscovite schist toward the east in the direction of increasing strain, possibly reflecting differences in bulk composition, fluid content, or metamorphism. For example, the grain sizes of samples RR91-59 (Indian Creek) and RR91-20 (Pine Creek), taken as representative of the east and west end of the shear zone, respectively, were compared by measurement in thin section. The difficulties in the determination of grain size from two-dimensional thin sections have been discussed by *Goodwin and Renne* [1991] and, while important, do not influence the relative grain size differences between samples. These differences in average grain size, which we interpret as repre-

Table 4. Selected Microprobe Analyses of Muscovite From the Elba Quartzite

	RR91-48	RR91-20	RR91-6	RR-83* Coarse	RR-83* Pull-Apart	RR91-114*
SiO_2	48.10	48.26	47.3	47.0	47.55	47.82
TiO_2	0.27	0.14	0.18	0.16	0.10	0.13
Al_2O_3	34.40	35.47	36.8	34.7	35.16	35.34
FeO	1.58	1.19	0.64	2 21	2.11	2 04
MnO	0.01	0.03	0.01	0.02	0.00	0.02
MgO	1.07	0.60	0.29	0.32	0.31	0.27
Na_2O	0 42	0.36	0.45	0.60	0.38	0.58
K_2O	10 87	10.46	10.32	10.2	9.75	10 04
H_2O calc	4.57	4.59	4.58	4.50	4.43	4.56
Total	101.29	101.10	100.57	99.77	99.92	100 80
			Formulas Based on 11 Oxygens			
Si	3.155	3.153	3.099	3.131	3.146	3.142
Ti	0.013	0.007	0.009	0.008	0.005	0.006
Al	2 659	2.731	2.841	2.728	2.743	2 737
Fe	0.087	0 065	0.035	0.123	0.117	0.112
Mn	0.001	0.002	0.001	0.001	0.000	0.001
Mg	0.105	0.058	0.028	0.032	0.031	0.027
Na	0.053	0.046	0.057	0.078	0.049	0 073
K	0.909	0.872	0.863	0.087	0.823	0.842
Cations	6.983	6.933	6.932	6.969	6.914	6.941
Mg#	54.7	47.2	44.4	20.5	20.7	19.3

Chemical analyses conducted with an ETEC Autoprobe with Krisel automation (wavelength dispersive system) at Northern Arizona University. Analyzed samples include both thin sections and grain mounts of mineral splits of those analyzed for Ar isotopes. Samples were analyzed with an accelerating voltage of 15 keV, a spot diameter of 10 μm and a 50 nA current. Natural minerals and synthetic materials were used as standards. Mg# = Mg/(Mg + Fe) x 100. Note that RR-83 is from same locality and horizon as Ar sample RR91-7.

* Samples from schistose, kyanite-bearing quartzite.

sentative, are 195 μm (Pine Creek) and 500 μm (Ten Mile Canyon). Furthermore, the analyzed grain size from the westernmost samples are smaller than those to the east (Table 1), also reflecting the differences in average natural grain size. Therefore the observed age variation cannot result from differing retentivity of muscovite of different grain size.

5.2. Composition

A further possible explanation for the $^{40}Ar/^{39}Ar$ intrasample and spatial age gradients is that they represent mixed ages, resulting from varying proportions of two or more compositionally distinct white mica populations of differing argon retentivity or of different ages. Compositional differences in white mica have been shown to influence argon retentivity [*Scaillet et al.*, 1992; *Roeske et al.*, 1995] and may be important in the interpretation of the mica age spectra. Microprobe analyses indicate no significant compositional difference between muscovite porphyroclasts and younger synkinematic muscovite (see sample RR83, Table 4). The microprobe data also rule out a compositional control on the difference in apparent ages between samples. No significant compositional difference is seen between samples, with the exception of a variation in Mg# (Mg# = (Mg/Mg+Fe) x 100) between the quartzites (RR91-48, RR91-20, RR91-6) and mica-quartz-kyanite schists (RR83, RR91-114). Importantly, no difference in age was noted between the quartz-mica-kyanite schists and quartzite (compare RR91-7 and RR91-6, Table 4).

5.3. Reheating

The suite of muscovite and biotite age spectra somewhat resemble argon loss profiles that could be produced by variable amounts of diffusive loss [*Turner*, 1968; *Dodson*, 1973] as a result of reheating at 15-10 Ma, following initial argon closure. To evaluate whether reheating could produce the suite of paired muscovite and biotite age spectra, we used the age spectra modeling program MacArgon [*Lister and Baldwin*, 1996]. This software uses a forward modeling approach to model the distribution of argon within the crystal lattice when subjected to an arbitrary P-T-t path. The modeling assumes that volume diffusion controls the distribution of argon within the mineral lattice and that the extraction of argon during the stepwise heating experiment also behaves according to volume diffusion. We recognize that the behavior of hydrous silicates probably departs from volume diffusion in a vacuum furnace during stepwise heating [*Gaber et al.*, 1988; *Lee et al.*, 1991]. With this in mind, we use the synthetic age spectra produced with MacArgon loosely as a check for the internal consistency between age spectra for minerals of differing retentivity (muscovite and biotite), subjected to the same thermal history. In addition, because the total gas ages of the model and laboratory analysis should correspond regardless of the extent to which the laboratory-induced degassing departs from that of the natural geologic environment, total gas ages can be compared between experiments and models.

Modeling of the family of muscovite apparent age spectra requires a minimum temperature differential between Century Hollow and Ten Mile Canyon of 125°C at 16 Ma for a reheating event of 1 m.y. or longer duration. The family of T-t reheating paths (Figure 12a) that satisfactorily reproduce the muscovite apparent age spectra (Figure 12c) cannot well reproduce the biotite age spectra (Figure 12f). Furthermore, the quartz microstructures indicate that deformation occurred during decreasing temperature conditions and outlasted elevated temperatures necessary for annealing recrystallization. Thus we interpret these data as representing differential cooling resulting from asymmetric extensional unroofing, rather than variable resetting due to reheating following deformation.

The morphology of the low-temperature portions of the muscovite and biotite age spectra for the western samples (Century Hollow and Pine Creek) are similar to apparent argon loss patterns produced by slight diffusive loss of radiogenic argon as a result of reheating [*Turner*, 1968; *Dodson*, 1973], with minimum ages ranging from 24 to 28 Ma (Figure 7). These samples are interpreted to record slight reheating related to the intrusion of Oligocene plutons present farther west in the Grouse Creek and southern Albion Mountains (Figure 1) [*Compton et al.*, 1977; *Forrest and Miller*, 1995; *Wells et al.*, 1997b].

In contrast, the age spectra for muscovite from the eastern samples (Fisher, Dunn, Indian, and Ten Mile Canyons) show significantly younger apparent argon loss patterns with low-temperature intercepts between about 9 and 13 Ma. It is unlikely that the apparent argon loss patterns result from reheating because cooling curves show cooling throughout the time interval of 20-7.5 Ma, down to temperatures below apatite fission track retention. The age gradients may alternatively record progressive growth of muscovite during extensional shearing. This is consistent with petrographic evidence for synextensional muscovite growth (Figure 5d). Corresponding temperatures derived from the cooling curves (250° to 300°C, Figures 11e and 11f) are also consistent with growth of new muscovite during ductile shearing at temperatures below muscovite closure. A similar interpretation from a contractional shear zone is described by *Kirschner et al.* [1996].

Age gradients are common in the high temperature gas fractions of the muscovite analyses and, to a lesser extent, the biotite analyses (Figure 7). These age gradients may represent degassing from more retentive grain cores, or possibly from mineralogically distinct inclusions, although none were noted either petrographically or from electron microprobe study. Alternatively, they may record excess argon housed in more retentive sites, similar to the large domain excess argon effect noted in alkali-feldspar [*Foster et al.*, 1990].

5.4. Variation in T-t Paths: Diachronous Cooling

The potential effect of variations in monotonic T-t paths in controlling the age variation between samples, rather than grain size, composition, or reheating as discussed above, was investigated using MacArgon [*Lister and Baldwin*, 1996] (Figure 12). T-t paths constructed using the previously discussed closure temperatures for the measured thermochronometers, and assuming monotonic cooling, were used as input for the forward modeling.

The synthetic age spectra for muscovite and biotite (Figure 12e, muscovite, and Figure 12h, biotite) agree remarkably well to a first order with the measured age spectra (Figure 12d, muscovite, and Figure 12g, biotite), providing confirmation, albeit not entirely independent, of the T-t paths determined by assuming a bulk closure temperature for individual mineral phases (Figure 12). The similarity between the synthetic and

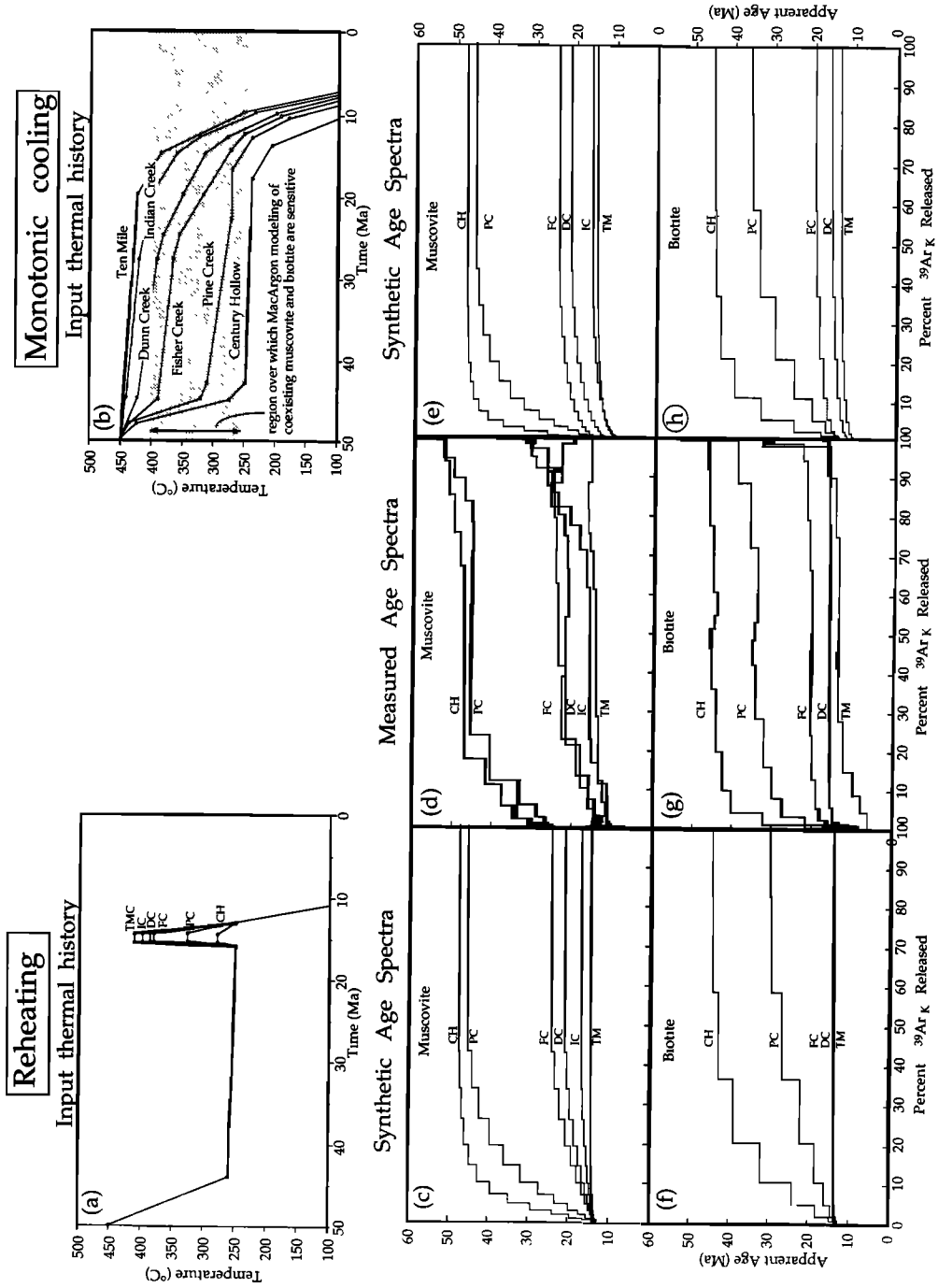

Figure 12. Evaluation of whether reheating or monotonic cooling best reproduces the family of muscovite and biotite apparent age spectra with the MacArgon program. Reheating magnitudes selected to best reproduce muscovite apparent age spectra. (a) Input reheating thermal history. (c) and (f) Simulated apparent age spectra for muscovite and biotite using input thermal histories of Figure 12a. (b) Input monotonic cooling histories. (e) and (h) Simulated apparent age spectra for muscovite and biotite using input thermal histories of Figure 12b. (d) and (g) Measured apparent age spectra for muscovite and biotite. The reheating thermal histories can not both reproduce the family of muscovite and biotite age spectra (note lack of similarity between simulated (Figure 12f) and measured (Figure 12g) biotite apparent age spectra for Fisher and Dunn Creek). The monotonic cooling histories well reproduce both the muscovite (compare Figure 12d to Figure 12e), and biotite (compare Figure 12g to Figure 12h) apparent age spectra.

measured apparent age spectra suggests that modeling the degassing mechanism as volume diffusion can reproduce in a general way the degassing behavior of the Raft River micas.

In summary, our interpretation of the flattish portions of the age spectra (20 to 80% ^{39}Ar released) is that they represent cooling ages through the bulk closure temperature interval. The spatial age gradients are interpreted to represent diachronous cooling of the shear zone, resulting from variations in thermal history with structural position during progressive asymmetric extensional exhumation. This is consistent with the overall shape and location-dependent differences for all composite cooling curves (Figure 11), which are similar to those predicted by thermal models [e.g., *Ketcham*, 1996] and those derived from other major normal fault systems [e.g., *Lee*, 1995].

6. Discussion

6.1. Dating of Deformation

Several approaches have been successfully used to date deformations that lack useful cross cutting relationships with younger rock units and a syntectonic sedimentary record. In rocks of lower greenschist facies metamorphic grade the dating of incipient metamorphism has been used to date the timing of cleavage formation if deformation is contemporaneous with prograde metamorphism [e.g., *Kligfield et al.*, 1986; *Reuter and Dallmeyer*, 1989]. At higher metamorphic grades, syn-kinematic growth of mineral phases with closure temperatures higher than deformation temperatures has been dated [e.g., *Getty and Gromet*, 1992; *Resor et al.*, 1996].

An alternative approach in dating deformation is to compare the empirical thermal history derived by thermochronological methods to the thermal history predicted by modeling the thermal response to a specified deformation. Using this approach, the dating of extensional shear zones is more tractable than the dating of contractional shear zones, principally because the syndeformational to postdeformational thermal history for extensional settings is simpler than for contractional settings. Peak temperatures may be achieved tens of millions of years after peak strain rates in contractional settings [e.g., *England and Thompson*, 1984], whereas decreasing temperature conditions typically accompany extensional deformation [*Rupple et al.*, 1988; *Ketcham*, 1996]. Thus, for regions where crustal thinning is the last major tectonic event, the cooling history can be linked to the extensional process, although the direct linkage depends on factors including fault geometry, rate of displacement, and geothermal gradient.

Two additional methods can be used in dating extensional deformation and are applied here. First, spatial gradients in cooling ages of detachment fault footwalls, in which cooling ages decrease in the hanging wall transport direction, can provide information on the timing of initiation and progressive extensional exhumation. Although some segments of spatial age gradients vary smoothly and may record the slip rate [*John and Foster*, 1993; *Foster et al.*, 1993], other segments exhibit abrupt steps in cooling age that can be used to delineate the timing of initiation of extensional tectonism [*John and Foster*, 1993]. Second, by integrating the temperature of deformation with the cooling history determined from thermochronology, the timing of deformation can be determined.

6.1.1. Age and extensional origin of low-temperature plastic shearing. The possibility that the shear zone in the footwall of the Raft River detachment may be a Mesozoic thrust zone [e.g., *Malavieille and Cobb*, 1986; *Snoke and Miller*, 1988] can be excluded in favor of a Miocene extensional origin, based on integration of cooling histories derived from eastern locations with temperature conditions implied by preserved microstructures (Figures 11d and 11e). As mentioned in section 2, quartz displays microstructures indicative of low-temperature plasticity at temperatures as low as 300-350°. Thermochronology of eastern localities shows that these rocks cooled through the 300-350°C temperature interval at about 14 to 12 Ma (depending on location), indicating plastic deformation during the Miocene (Figures 11d and 11e), compatible with crustal extension. Furthermore, the similarity of the overall shape and location-dependent differences for all composite cooling curves (Figure 11) to those predicted by thermal models [e.g., *Ketcham*, 1996] and those derived from other major normal fault systems [e.g., *Lee*, 1995] and the relatively rapid cooling rate during mylonitic shearing are most compatible with extensional, rather than contractional, processes. Decreasing temperature conditions leading to cataclasite formation occurred during unidirectional shearing, further linking the Miocene brittle fault to the underlying ductile shear zone.

The cooling curves detail the progression from temperatures permissive of plastic shearing to those of brittle faulting. For example, the cooling curve for Ten Mile Canyon indicates passage through this transition (~275° to 325°C) at about 12 to 10 Ma (Figure 11f). The lack of penetrative deformation of a 10 Ma diabase sill intruded along the detachment fault is consistent with the progression from distributed ductile to localized brittle shearing by this time.

The crystal-plastic fabric in quartzite at Century Hollow and Pine Creek is interpreted to be associated with mylonitic fabric displayed at eastern localities (e.g., Ten Mile Canyon) that developed as recently as 14-12 Ma. Muscovite and biotite cooling ages at Century Hollow and Pine Creek (Figure 7), however, are significantly older than the middle Miocene mylonitic deformation, indicating low-T plasticity of quartz at temperatures lower than both muscovite and biotite closure (~300-350°C). This is consistent with inferred temperatures from slip system inferences.

6.1.2. Age of inception of Miocene extension. Spatial gradients in cooling ages, in which cooling ages decrease in the hanging wall transport direction, have been documented in a number of detachment fault footwalls [e.g., *Lee and Sutter*, 1991; *Richard et al.*, 1990; *Holm et al.*, 1992; *John and Foster*, 1993; *McGrew and Snee*, 1994; *Hoisch et al.*, 1997a]. In general, they are interpreted to record progressive unroofing and cooling as the footwalls are progressively drawn out from beneath extending hanging walls.

Abrupt steps in cooling age on age versus distance plots can be used to delineate the timing of initiation of extensional tectonism, following the approach used by *John and Foster* [1993]. Figure 13a shows a hypothetical preextensional faulting geometry and distribution of samples. Samples A and B lie above the closure interval for argon diffusion, sample C lies within the closure interval, and samples D, E, and F lie below the closure interval. After extensional shearing and exhumation the following cooling age distribution would be recorded (Figure 13b): samples A and B would record preextensional cooling; samples D, E, and F would record

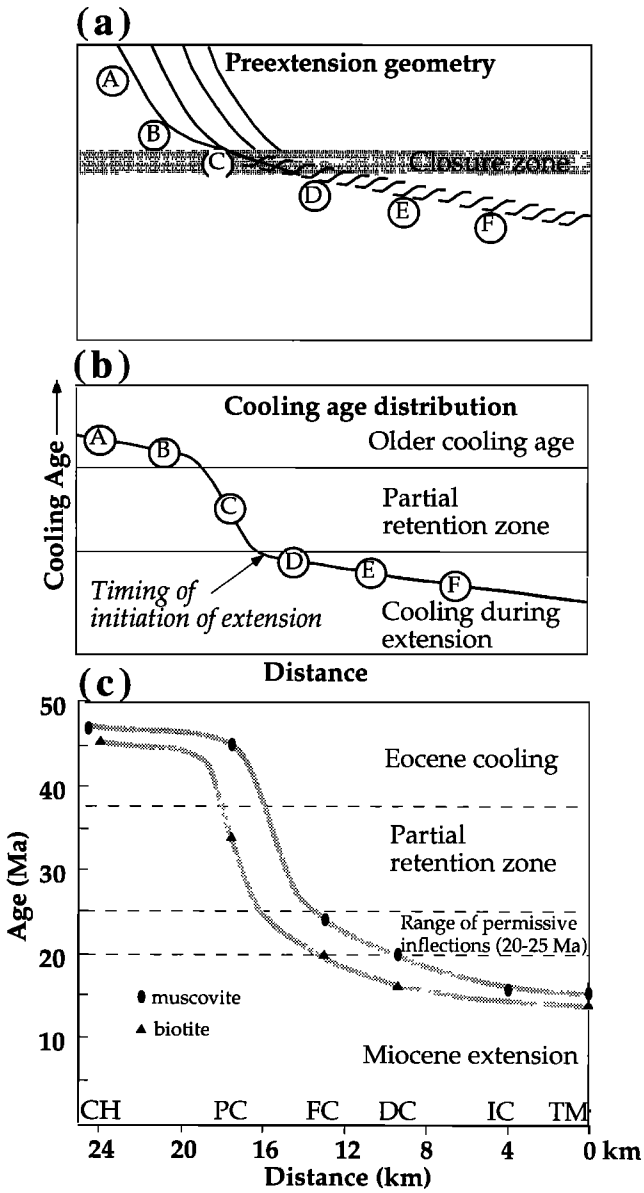

Figure 13. (a) Cross section illustrating prefaulting location of hypothetical samples along a detachment fault system. (b) Idealized cooling age distribution as shown on an age versus distance plot. Note that inflection (arrow) marks the timing of initiation of cooling due to extension and that the slope of the line segment D-F is equal to the inverse of the slip rate. (c) Age versus distance plot for muscovite and biotite apparent ages across the central and eastern Raft River Mountains. Distances are measured parallel to the transport direction. Inflection is not well defined but permits a range in permissive inflections of 20 to 25 Ma. CH, Century Hollow; DC, Dunn Creek; FC, Fisher Creek; IC, Indian Creek; PC, Pine Creek; TM, Ten Mile Canyon.

cooling during extensional exhumation; and sample C would record an intermediate age between B and D, due to incomplete argon loss and partial retention, or slow cooling through the closure interval. Importantly, the inflection in cooling ages between C and D would mark the age of initiation of extensional denudation. This approach does not require that the initiation of extension coincide with the onset of rapid cooling. The inflection will mark the onset of extension as long as there is a component of absolute cooling as rocks undergo decompression.

The muscovite and biotite $^{40}Ar/^{39}Ar$ apparent ages from the Raft River Mountains are shown in Figure 13c as a plot of cooling age versus lateral distance measured parallel to the shear zone boundary and in the transport direction. Muscovite and biotite from Century Hollow and muscovite from Pine Creek record Eocene cooling and are interpreted to have occupied a position above their respective closure interval prior to Miocene extension. Muscovite and biotite from Fisher, Dunn, Indian, and Ten Mile Creek Canyons are interpreted to have resided at structural levels beneath their respective closure intervals prior to Miocene extension, and their recorded spatial age progression is interpreted to record progressive cooling through the closure interval during extensional denudation. Biotite from Pine Creek Canyon is interpreted to have resided within its partial retention zone between the Eocene and Miocene. The inflections in the apparent age versus lateral distance curves for muscovite and biotite are not tightly constrained. However, they do permit a range of permissible inflections between about 25 and 20 Ma. Thus the age of initiation of extension in the Miocene, as recorded in the spatial distribution of mica cooling ages, is bracketed between about 25 and 20 Ma and could be refined with a closer spacing between samples.

6.2. Eocene Extension

Eocene cooling is best recorded in the western sample localities, and thermal histories from Century Hollow and Pine Creek show an early rapid cooling event from >47 Ma to <45 Ma (Figures 11a and 11b). MacArgon modeling of muscovite and biotite $^{40}Ar/^{39}Ar$ age spectra allows the magnitude and rate of cooling to be better constrained. A minimum cooling rate of 20°C/m.y. is required to preserve a 2.0 m.y. age difference between muscovite and biotite, assuming that the temperature did not decrease below 250°C in Eocene time (Figures 14a and 14b); relaxing this constraint decreases the cooling rate slightly. This assumption is consistent with all data, including the requirement of elevated temperature for plastic behavior of quartz in Miocene mylonite. The 20°C/m.y. cooling rate is increased significantly if the isochron analyses for biotite RR91-51 (46.5 Ma) is accepted, rather than the "preferred age" (45.2 Ma), which allows only a 1 m.y. age differential. The extent of cooling was parametrically modeled to determine the maximum temperature required to close biotite to subsequent, significant diffusional argon loss and preserve the Eocene age (Figures 14c and 14d).

Middle Eocene cooling is interpreted to result from unroofing of the footwall to the top-to-the-WNW Middle Mountain extensional shear zone present on the west side of the Grouse Creek, Raft River, and Albion Mountains [*Saltzer and Hodges*, 1988; *Wells et al.*, 1997b] (Figure 15a) by a mechanism similar to that proposed for footwall rotational tilting by *Wernicke and Axen* [1988]. Middle to late Eocene extensional denudation along the Middle Mountain shear zone produced an eastward dip to rocks presently in the footwall of the Raft River detachment prior to Miocene extension. The eastward dip is reflected in differences in temperature and apparent structural depth at the same stratigraphic level between the east and west ends of the sampled transect prior to Miocene extension. An Eocene age

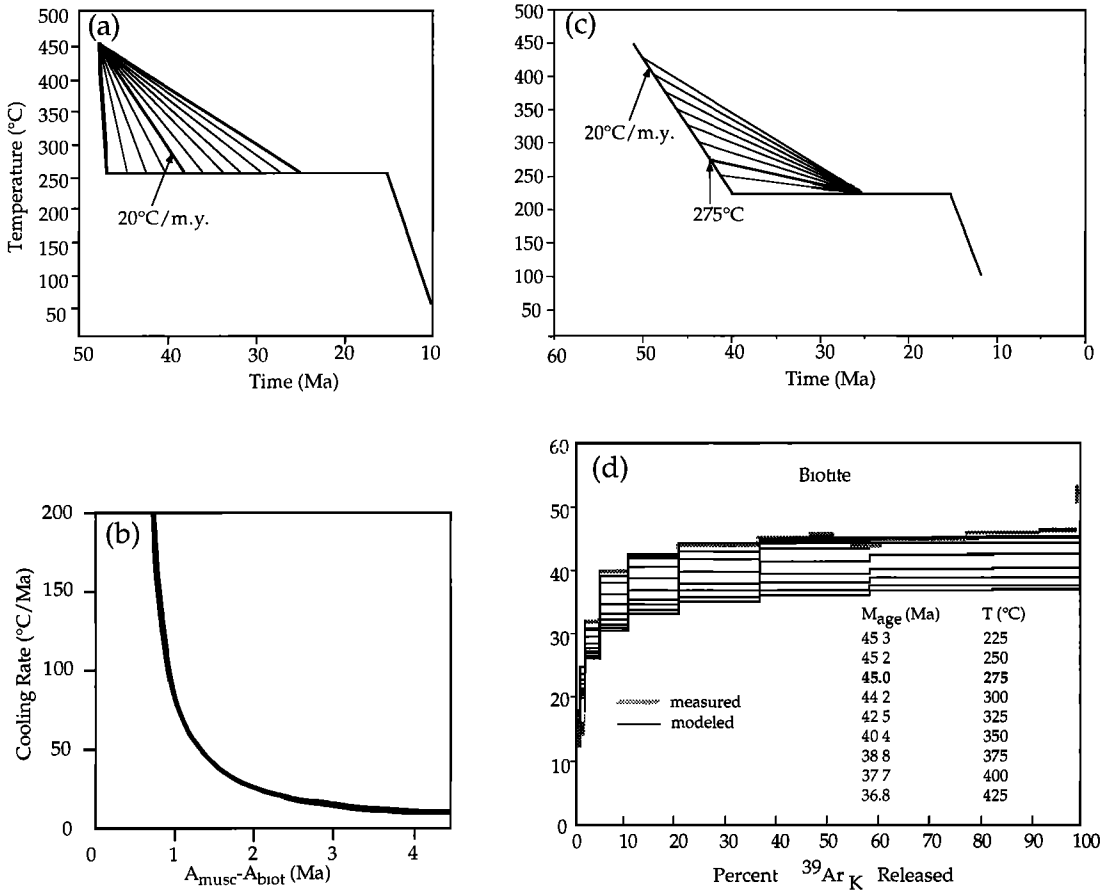

Figure 14. MacArgon parametric modeling of the rate and extent of Eocene cooling, using muscovite (RR91-48) and biotite (RR91-51) apparent age spectra from Century Hollow. (a) Parametric thermal models used to determine the cooling rate. (b) Summary of the difference in ages between model muscovite and biotite apparent age spectra resulting from thermal histories of Figure 14a for different cooling rates. The measured age differential (2.0 m.y., A_{musc}-A_{biot}) between muscovite and biotite $^{40}Ar/^{39}Ar$ analyses from Century Hollow indicates a minimum cooling rate of 20°C/m.y. (c) and (d) Modeling of the extent of moderate to rapid cooling required to preserve an Eocene age, constrained by analysis of least retentive phase, biotite. Figure 14c shows input thermal histories for Figure 14d; Figure 14d shows modeled age spectra for biotite compared to measured biotite analysis (RR91-51). M_{age}(Ma) of Figure 14d is maximum age, T(°C) is temperature of endpoint of 20°C/m.y. cooling cord. Model requires cooling at ≥20°C/m.y. to ≤275°C.

for early shearing along the Middle Mountain shear zone has been confirmed by muscovite cooling ages of 42 to 37 Ma from mylonitic rocks deformed at upper greenschist facies conditions [*Wells et al.*, 1997b].

Following middle Eocene cooling, the western localities show a relatively constant temperature throughout the Oligocene, with permissive slight reheating associated with intrusions farther west, and rapid and accelerating cooling during the Miocene. In contrast, the central and eastern Raft River Mountains show an apparent single progressive cooling history in the Miocene (Figures 11d-11f); however, the lack of apparent Eocene cooling may be due to the poor resolution of the higher-temperature part of the thermal history. The hornblende data, due to extraneous ^{40}Ar, only conservatively provide maximum ages as low as 54 Ma, and thus the portions of the cooling curves of higher temperature than muscovite closure are poorly constrained. However, the lack of plasticity of feldspar implies temperatures less than ~450°C during Miocene extensional shearing, which when combined with the 54 Ma maximum age, suggests that hornblende may have closed to argon diffusion during Eocene cooling.

6.3. Late Oligocene-Early Miocene Extension

Late Oligocene-early Miocene extension is indicated by the initiation of cooling evident from the Fisher and Dunn Creek localities and by the inflection in the age versus distance plot for muscovite and biotite $^{40}Ar/^{39}Ar$ apparent ages. Although the middle to late Miocene cooling history of the Raft River Mountains clearly records tectonic denudation along the top-to-the-east Raft River detachment fault and shear zone, it is less certain whether the late Oligocene to early Miocene cooling is related to top-to-the-east extensional shear and, if so, whether the shearing is episodic or continuous.

Latest Oligocene to early Miocene cooling (25-20 Ma) may be entirely unrelated to the Raft River detachment and associated solely with the top-to-the-west Middle Mountain

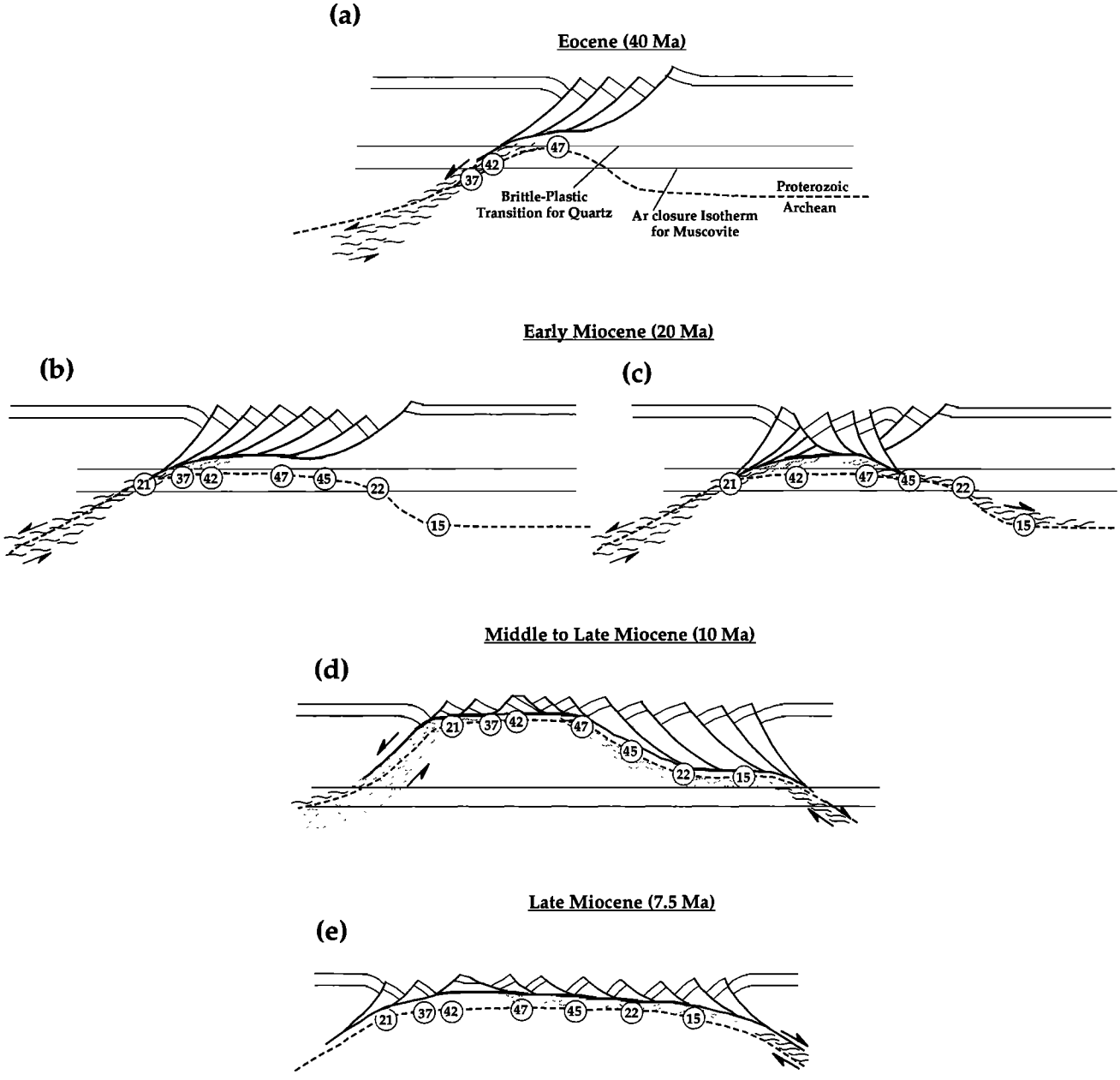

Figure 15. Schematic kinematic sequence of extensional exhumation along two oppositely vergent extensional shear zone and detachment fault systems illustrating the progressive kinematic transition from a west rooted extensional system to an east rooted one. Numbers in parentheses beside time frames indicate specific time for which schematic sections were constructed. Circled numbers refer to muscovite total gas ages: those to west of Century Hollow are from *Wells et al.* [1997b]. Late Oligocene to early Miocene cooling recorded in muscovite $^{40}Ar/^{39}Ar$ ages in the central Raft River Mountains may have resulted from either the top-to-the-west Middle Mountain shear zone (Figure 15b) or principally the top-to-the-east Raft River shear zone (Figure 15c), which requires simultaneous motion on both oppositely rooted shear zones. Upper plate structure is schematic and not intended to balance but rather to illustrate the active dip domains.

shear zone along the western margin of the Raft River, Grouse Creek, and Albion Mountains (Figure 15b). Preliminary thermochronology and structural analysis from the northern Grouse Creek and western Raft River Mountains indicate an episode of rapid cooling at 25 to 20 Ma, associated with top-to-the-west motion along the Middle Mountain shear zone at greenschist facies, and deformation of late Oligocene granite [*Miller et al.*, 1983; *Forrest and Miller*, 1995; *Wells et al.*, 1997a,b]. This latest Oligocene to early Miocene shearing overprints early top-to-the-WNW motion at upper greenschist to amphibolite facies [*Saltzer and Hodges*, 1988; *Wells et al.*, 1997b]. However, we favor a link between latest Oligocene to early Miocene cooling in the central Raft River Mountains and early motion along the Raft River detachment and shear zone because substantial cooling between 25 and 20 Ma is not permitted at the Pine Creek locality (despite the

discrepancy between the MacArgon model for muscovite and biotite and the K-feldspar model, Figure 11b), and Pine Creek is significantly closer to the west vergent Middle Mountain shear zone than the Fisher and Dunn Creek localities (Figure 1). If this interpretation is correct, then simultaneous tectonic denudation along both oppositely vergent shear zone systems [e.g., *Malavieille*, 1993] (Figure 15c) probably occurred early in the history of the Raft River detachment.

Several aspects of the spatial and temporal pattern of late Oligocene to early Miocene cooling depart from that expected along a single and simple detachment fault footwall [*Wernicke and Axen*, 1988; *Ketcham*, 1996] and may reflect a more complicated fault geometry with either multiple ramps, two periods of motion, or simultaneous and nonuniform hanging wall thinning. The age of initiation of rapid cooling, as defined by K-feldspar modeling, gets progressively younger from Pine Creek to Ten Mile Canyon, as expected given the asymmetry of exhumation. However, the age of initial cooling departs from this pattern; the age of initial cooling gets older from Ten Mile Canyon to Fisher Creek, but the well-defined time of initiation of cooling at Pine Creek is substantially younger. Two extensional events may be indicated rather than one: a first event that corresponds to the 25-20 Ma initiation of extension as determined from the mica spatial age gradient and the onset of cooling at Fisher and Dunn Creeks, and a second event recorded in the onset of rapid cooling at Pine Creek (16-15 Ma). This could result from early motion along a fault that departs from the stratigraphic level of the Elba Quartzite and ramps upsection above and near the location of Fisher Creek, such that the locations between Fisher Creek and Ten Mile Canyon experienced progressive cooling related to this early period of movement. In such a scenario, at about 16 Ma the detachment may have cut headward into its footwall, perhaps due to continued unroofing and rotation of strata in the footwall of the Middle Mountain shear zone, and captured a large region to the west in a backward breaking kinematic progression, such that cooling is initiated in the Pine Creek and Century Hollow locations.

Alternatively, the time lag of ~4 to 9 m.y between the age of onset of rapid cooling at Pine Creek (16-15 Ma) and the onset of extension (25-20 Ma) may result from a single extensional phase. A time lag between cooling and extension is predicted for rocks that are initially beneath flat or very low-angle dipping segments of detachment faults that steepen toward the surface, simply due to their greater vertical component of displacement through time. Additionally, a time lag is indicated by recent thermal models because the cooling of the footwall does not keep pace with fault displacement under certain conditions of slip rate and fault geometry [*Ketcham*, 1996; *Hoisch et al.*, 1997b]. The difference between cooling histories of the western and eastern localities may reflect the presence of two ramps in the detachment fault/shear zone system: an upper crustal ramp defining the breakaway fault and a midcrustal ramp. In this scenario, only the eastern localities would have experienced cooling related to motion up the midcrustal ramp, whereas both the eastern localities and Pine Creek would record cooling due to the structurally higher ramp. Furthermore, the geometry of the fault and its evolution through time may be governed by nonuniform, simultaneous hanging wall thinning, with isostatic rebound and consequent cooling closely tracking hanging wall thinning (Figure 15d).

6.4. Middle to Late Miocene Raft River Detachment

The spatial and temporal variations in middle to late Miocene cooling (Figures 12b and 13c) are consistent with footwall exhumation along the east dipping Raft River detachment fault and footwall shear zone (Figures 15d and 15e). Middle to late Miocene cooling rates average ~30°C/m.y. Modeled track length distributions and synoptic cooling curves show an acceleration in cooling rate during extension, to rates of 70 to 100°C/m.y. (Figure 11), consistent with modeled convex upward cooling curves for detachment fault footwalls [*Ketcham*, 1996; *Hoisch et al.*, 1997b].

Apatite fission track ages are progressively younger toward the east (Figure 16) and document the progressive

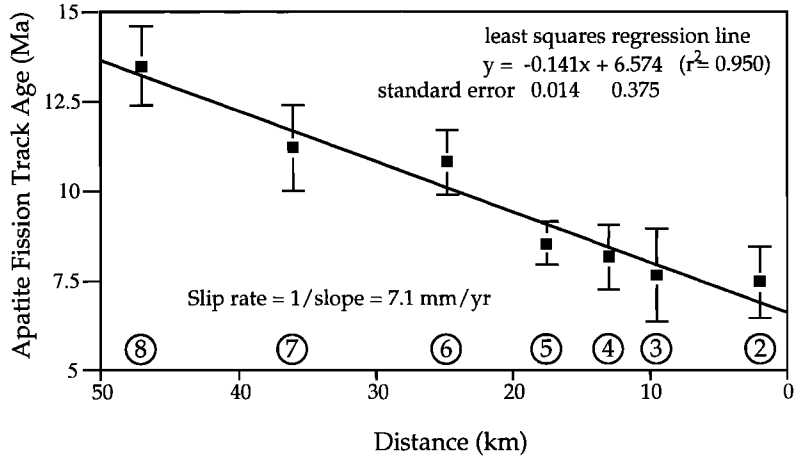

Figure 16. Age versus distance plot of apatite fission track analyses, with 1σ errors indicated. Distance is measured parallel to the base of the shear zone and the hanging wall transport direction. Least squares linear regression yields a line whose slope yields a slip rate of 7 mm/yr (+0.8, -0.7 at standard error). Fission tracks of all samples were measured "blind" with respect to location by AEB. Circled numbers refer to sample locations of Figure 1.

exhumation by the Raft River detachment fault, as the footwall rocks progressively pass through the effective temperature interval for fission track retention. Similar systematic relationships between cooling age and distance measured parallel to the transport direction have been noted from other detachment fault footwalls and have been interpreted to record the slip rate for the bounding fault [*Foster et al.*, 1993]. The assumptions in this technique are that cooling is solely a result of the vertical component of fault displacement, and that isotherms are immobile [*Ketcham*, 1996]. The second assumption is most easily met with low-temperature thermochronometry such as apatite fission track. The first assumption, however, is strictly valid if there is no extension within the hanging wall. Where hanging wall thinning occurs in a systematic fashion according to the rolling hinge model [*Buck*, 1988; *Wernicke and Axen*, 1988], this method will overestimate the slip rate because the pattern of cooling ages will result from combined fault-parallel displacement and isostatic/flexural uplift resulting from thinning of the hanging wall. The final width of extended hanging walls, measured parallel to the detachment fault, approximates the sum of the initial length of the hanging wall and the cumulative slip. The less extended the hanging wall, the greater the overestimation of slip by this thermochronological method. Therefore the rate of migration of the hinge, not the slip rate on the master fault, is determined, and the rate of hinge migration will exceed the slip rate along the fault. For example, horizontal extension of the hanging wall of 200% results in overestimation of the slip rate by ~50%, and this discrepancy between slip rate and hinge migration rate is reduced with increasing values of hanging wall extension. Therefore the determined rate should be cautiously interpreted as an apparent slip rate.

Linear regression of the apatite fission track data on an age versus lateral distance plot [*Foster et al.*, 1993] indicates an apparent slip rate of ~7 mm/yr (+0.8, -0.7 at standard error) (Figure 16). Apparent slip rates similarly determined along regionally extensive low-angle normal faults from other studies, principally in the Colorado River trough region of the western United States, are 3 mm/yr (South Mountain [*Fitzgerald et al.*, 1993]); 3 to 7 mm/yr (Chemehuevi Mountains [*John and Foster*, 1993]); 5 to 8 mm/yr (Naxos, Greece [*John and Howard*, 1995]); and 7 to 9 mm/yr (Huacuvar, Buckskin and Rawhide Mountains [*Foster et al.*, 1993] and Whipple Mountains [*Davis and Lister*, 1988; *Spencer and Reynolds*, 1991]). The calculated 7 mm/yr apparent slip rate for the Raft River detachment fault from apatite fission track data is similar to these other estimates of apparent slip rates along regionally extensive low-angle normal faults both in the Basin and Range and extensional provinces worldwide. However, without integration of the amount of extension of the hanging wall, a difficult value to access in the Raft River Mountains due to poor preservation (Figure 2), it should be treated as a maximum because of the likelihood that the first assumption of above is not satisfied.

Miocene volcanic and sedimentary rocks in the Raft River Valley provide additional constraints on the timing of detachment faulting. Miocene rocks in the Jim Sage and Cottrell Mountains of the western Raft River Valley (Figure 1) are generally west dipping and are interpreted to lie in the hanging wall of the Raft River detachment fault [*Covington*, 1983; *Miller et al*, 1983]. Rhyolite and olivine basalt in the northern Cottrell Mountains have been dated by K-Ar at 9.2 ± 0.5 and 10.2 ± 1.5 Ma, respectively [*Armstrong*, 1975, 1976]. These relations indicate that movement along the detachment continued following deposition of 10 to 9 Ma volcanic rocks, consistent with rapid cooling at this time as indicated by the thermochronology (Figure 11). The cooling curves from the eastern Raft River Mountains (Figures 11e and 11f) imply that motion along the Raft River detachment lasted until 7.4 Ma or younger. Dating of post-tectonic basalts that unconformably overlie folded Miocene sedimentary rocks (Salt Lake Formation) in the Curlew Valley to the east may provide a better upper age limit for detachment fault motion in the subsurface to the east.

7. Conclusions

1. Cenozoic cooling of the Precambrian rocks in the Raft River Mountains was related to two geographically and chiefly temporally distinct, oppositely rooted extensional shear zone and detachment fault systems, the east rooted Raft River detachment and shear zone and the west rooted Middle Mountain shear zone.

2. Extension along the top-to-the-westnorthwest Middle Mountain shear zone initiated in middle Eocene time. Motion along the top-to-the-east Raft River detachment initiated in late Oligocene to early Miocene time. Although the timing of deformation along these oppositely rooted shear zones may have overlapped late in the movement history of the Middle Mountain shear zone and early in the movement history of the Raft River detachment, much of the extensional exhumation along these shear zones was temporally distinct. This improved chronology suggests that the Raft River-Grouse Creek-Albion metamorphic core complex should not be viewed as a type example for simultaneous symmetric bivergent extension [e.g., *Malavieille*, 1993] because bivergent extension represented but a brief period of overlap between two asymmetric detachment fault systems.

3. An apparent slip rate for the Raft River detachment of 7 mm/yr, over the time interval of 13.5 to 7.4 Ma, is determined by apatite fission track analyses. This rate is comparable to those determined from other detachment faults, by similar techniques, in continental extensional environments. The apparent slip rate is interpreted as the rate of migration of the leading edge of the domal uplift or rolling hinge and is faster than the true slip rate for the detachment fault.

4. Plastic deformation of quartz significantly postdates muscovite and biotite $^{40}Ar/^{39}Ar$ cooling ages in the western localities, suggesting that deformation mechanisms and inferred temperatures need to be adequately characterized to properly interpret mica ages from low-temperature mylonites.

5. Integration of deformation temperatures with cooling histories indicates ages of deformation of early to middle Miocene for the Raft River shear zone. In general, this approach provides a useful method to date extensional ductile shear zones.

Acknowledgments. This study was supported by the National Research Council Postdoctoral Fellowship Program (M.L.W.), the U.S. Geological Survey, and the National Science Foundation (grant EAR-9317387 to M.L W.). We thank David M. Miller for providing logistical support and encouragement, Ross Yeoman and Steven Harlan for assistance in argon isotopic analysis, and Jim Wittke for electron microprobe analyses. Gordan Lister is thanked for freely providing the MacArgon program and Oscar Lovera for the K-feldspar modeling

software. Constructive reviews by Keith Howard, Elizabeth Miller, and Gene Smith improved the original manuscript and are greatly appreciated.

References

Applegate, J.D.R., J.D. Walker, and K.V. Hodges, Late Cretaceous extensional unroofing in the Funeral Mountains metamorphic core complex, California, *Geology, 20*, 519-522, 1992.

Armstrong, R.L., Mantled gneiss domes in the Albion Range, southern Idaho, *Geol. Soc. Am. Bull., 79*, 1295-1314, 1968.

Armstrong, R.L., The geochronometry of Idaho, part 1, *Isochron West, 14*, 1-50, 1975.

Armstrong, R.L., The geochronometry of Idaho, part 2, *Isochron West, 15*, 1-33, 1976.

Armstrong, R.L., J F. Smith, H.R Covington Jr., and P.L. Williams, Preliminary geologic map of the west half of the Pocatello 1° x 2° quadrangle, Idaho, scale 1:250,000, *U S Geol. Surv. Open File Rep. 78-533*, 1978.

Buck, W. R, Flexural rotation of normal faults, *Tectonics, 7*, 959-973, 1988.

Burchfiel, B.C., D C. Cowan, and G.A. Davis, Tectonic overview of the Cordilleran orogen in the western United States, in *The Geology of North America*, vol. G3, *The Cordilleran Orogen: Conterminous U.S.*, edited by B.C. Burchfiel, P.W. Lipman, and M.L. Zoback, pp. 407-479, Geol. Soc. of Am., Boulder, Colo., 1992

Compton, R. R., Geologic map of Yost quadrangle, Box Elder County, Utah, and Cassia County, Idaho, *U.S. Geol. Surv. Misc. Geol. Invest. Map, I-672*, 1972.

Compton, R. R., Geologic map of Park Valley quadrangle, Box Elder County, Utah, and Cassia County, Idaho, *U.S. Geol Surv Misc. Geol. Invest Map, I-873*, 1975.

Compton, R. R., Fabrics and strains in quartzites of a metamorphic core complex, Raft River Mountains, Utah, in *Cordilleran Metamorphic Core Complexes*, edited by M.D Crittenden, P.J Coney Jr, and G.H. Davis, *Mem. Geol Soc. Am 153*, 385-398, 1980.

Compton, R. R., Displaced Miocene rocks on the west flank of the Raft River-Grouse Creek core complex, Utah, in *Tectonic and Stratigraphic Studies in the Eastern Great Basin*, edited by D.M. Miller, V.R. Todd, and K.A Howard, *Mem Geol Soc. Am, 157*, 271-279, 1983.

Compton, R. R., V. R. Todd, R. E. Zartman, and C. W Naeser, Oligocene and Miocene metamorphism, folding, and low-angle faulting in northwestern Utah, *Geol. Soc Am. Bull., 88*, 1237-1250, 1977.

Coney, P.J., and T.A. Harms, Cordilleran metamorphic core complexes: Cenozoic extensional relics of Mesozoic compression, *Geology, 12*, 550-554, 1984.

Covington, H.R., Structural evolution of the Raft River Basin, Idaho, in *Tectonic and Stratigraphic Studies in the Eastern Great Basin*, edited by Miller, D. M., V. R. Todd, and K. A. Howard, *Mem. Geol. Soc Am., 157*, 229-237, 1983.

Crittenden, M D., Jr., Oligocene and Miocene metamorphism, folding, and low-angle faulting in northwestern Utah, Discussion, *Geol. Soc. Am. Bull., 90*, 305-306, 1979.

Crittenden, M.D., Jr., P.J. Coney, and G.H. Davis, editors, Cordilleran metamorphic core complexes, *Mem. Geol Soc Am., 153*, 490 pp., 1980.

Dalrymple, G.B., E C. Alexander, M A. Lanphere, and G.P. Kraker, Irradiation of samples for $^{40}Ar/^{39}Ar$ dating using the Geological Survey TRIGA reactor, *U.S. Geol Surv. Prof. Pap, 1176*, 56 pp., 1981.

Davis, G.A., and G.S. Lister, Detachment faulting in continental extension: Perspectives from the southwestern U.S. Cordillera, in *Processes in Continental Lithospheric Deformation*, edited by S.P. Clark, *Spec. Pap. Geol. Soc. Am., 218*, 133-159, 1988.

Dodson, M.H., Closure temperature in cooling geochronological and petrological systems, *Contrib Mineral. Petrol., 40*, 259-274, 1973.

Dokka, R.K., M J. Mahaffie, and A.W Snoke, Thermochronologic evidence of a major tectonic denudation associated with detachment faulting, northern Ruby Mountains-east Humboldt Range, Nevada, *Tectonics, 5*, 995-1006, 1986.

England, P C., and A.B. Thompson, Pressure-temperature-time paths of regional metamorphism, I, Heat transfer during the evolution of regions of thickened continental crust, *J. Petrol., 25*, 894-928, 1984.

Etheridge, M.A., V.J. Wall, and S.F. Cox, High fluid pressures during regional metamorphism and deformation: Implications for mass transport and deformation mechanisms, *J. Geophys Res., 89*, 4344-4358, 1984

FitzGerald, J.D., and H. Stunitz, Deformation of granitoids at low metamorphic grade, I, Reactions and grain size reduction, *Tectonophysics, 221*, 299-324, 1993.

Fitzgerald, P.G., and A.J.W. Gleadow, Fission track geochronology, tectonics and structure of the Transantarctic Mountains in northern Victoria Land, Antarctica, *Chem. Geol, 73*, 169-198, 1988.

Fitzgerald, P.G., S.J. Reynolds, E. Stump, D.A. Foster, and A.J.W. Gleadow, Thermochronological evidence for timing and denudation and rate of crustal extension of the South Mountains metamorphic core complex and Sierra Estrella, Arizona, *Nucl. Tracks Radiat. Meas., 21*, 555-563, 1993.

Forrest, S. D., and E.L. Miller, Oligocene plutonism and associated crustal thinning in the southern Albion Mountains, Idaho, *Geol. Soc. Am. Abstr Programs, 26*, A192, 1995.

Foster, D.A., T.M Harrison, P. Copeland, and M T. Heizler, Effects of excess argon within large diffusion domains on K-feldspar age spectra, *Geochim. Cosmochim. Acta, 54*, 1699-1707, 1990.

Foster, D.A., A.J W. Gleadow, S J. Reynolds, and P.G. Fitzgerald, Denudation of metamorphic core complexes and the reconstruction of the transition zone, west central Arizona: Constraints from apatite fission track thermochronology, *J. Geophys. Res., 98*, 2167-2185, 1993.

Foster, D.A., B.P. Kohn, and A.J W. Gleadow, Sphene and zircon fission track closure temperatures revisited. empirical calibrations from $^{40}Ar/^{39}Ar$ diffusion studies of K-feldspar and biotite, paper presented at 8th International Workshop of Fission Track Thermochronology, Univ of Ghent, Ghent Belgium, Aug 26-30, 1996.

Gaber, L.J., K.A. Foland, and C E. Corbato, On the significance of argon release from biotite and amphibole during $^{40}Ar/^{39}Ar$ vacuum heating, *Geochim. Cosmochim. Acta, 52*, 2457-2465, 1988.

Gallagher, K, Evolving temperature histories from apatite fission-track data, *Earth Planet Sci. Lett., 136*, 421-435, 1995

Geissman, J W., L W. Snee, G.W. Graaskamp, R B. Carten, and E.P. Geraghty, Deformation and age of the Red Mountain intrusive system (Urad-Henderson molybdenum deposits), Colorado: Evidence from paleomagnetic and $^{40}Ar/^{39}Ar$ data, *Geol. Soc Am Bull., 104*, 1031-1047, 1992.

Getty, S.R, and L.P. Gromet, Geochronological constraints on ductile deformation, crustal extension, and doming about a basement-cover boundary, New England Appalachians, *Am. J. Sci, 292*, 359-397, 1992.

Gleadow, A.J.W., and P G. Fitzgerald, Uplift history and structure of the Trans-Antarctic Mountains: New evidence from fission track dating of basement apatites in the Dry Valleys area, Southern Victoria Land, *Earth Planet. Sci. Lett, 82*, 1-14, 1987.

Gleadow, A.J.W., I.R Duddy, P. F. Green, and J. F. Lovering, Confined fission track lengths in apatite: A diagnostic tool for thermal history analysis, *Contrib. Mineral. Petrol., 94*, 405-415, 1986

Goodwin, L B., and P.R. Renne, Effects of progressive mylonitization on Ar retention in biotites from the Santa Rosa mylonite zone, California, and thermochronologic implications, *Contrib Mineral Petrol., 108*, 283-297, 1991.

Hames, W E, and S.A. Bowring, An empirical evaluation of the argon diffusion geometry in muscovite, *Earth Planet. Sci. Lett., 124*, 161-169, 1994.

Harrison, T.M, Diffusion of ^{40}Ar in hornblende, *Contrib Mineral. Petrol., 78*, 324-331, 1981.

Harrison, T.M., and I. McDougall, Excess ^{40}Ar in metamorphic rocks from Broken Hill, New South Wales: Implications for $^{40}Ar/^{39}Ar$ age spectra and the thermal evolution of the regions, *Earth Planet. Sci. Lett, 55*, 123-149, 1981.

Harrison, T.M, I Duncan, and I. McDougall, Diffusion of ^{40}Ar in biotite: Temperature, pressure and compositional effects, *Geochim. Cosmochim. Acta, 49*, 2461-2468, 1985

Harrison T.M., M.T. Heizler, O.M. Lovera, W Chen, and M. Grove, A chlorine disinfectant for excess argon released from K-feldspar during step heating, *Earth Planet Sci. Lett., 123*, 95-104., 1994.

Hoisch, T.D., M.T. Heizler, and R.E. Zartman, Timing of detachment faulting in the Bullfrog Hills and Bare Mountain area, southwest Nevada: Inferences from $^{40}Ar/^{39}Ar$, K-Ar, U-Pb, and fission track thermochronology, *J Geophys Res., 102*, 2815-2833, 1997a.

Hoisch, T.D., M.L Wells, and E. Wolff, Two-dimensional thermal

models of detachment faulting, with application to the Raft River detachment in northwest Utah, *Geol. Soc. Am. Abstr. Programs, 29*, A381, 1997b.

Holm, D.K., J.K. Snow, and D.R Lux, Thermal and barometric constraints on the intrusion and unroofing history of the Black Mountains: Implications for timing, initial dip, and kinematics of detachment faulting in the Death Valley region, *Tectonics, 11*, 507-522, 1992.

Hurford, A. J., and P.F Green, The zeta age calibration of fission track dating, *Isotope Geosci., 1*, 285-317, 1983.

John, B.E., and D.A Foster, Structural and thermal constraints on the initiation angle of detachment faulting in the southern Basin and Range: The Chemehuevi Mountains case study, *Geol. Soc. Am. Bull., 105*, 1091-1108, 1993.

John, B.E., and K.A. Howard, Rapid extension recorded by cooling-age patterns and brittle deformation, Naxos, Greece, *J. Geophys Res., 100*, 9969-9979, 1995.

Ketcham, R.A , Thermal models of core-complex evolution in Arizona and New Guinea. Implications for ancient cooling paths and present-day heat flow, *Tectonics, 15*, 933-951, 1996.

Kirschner, D.L., M.A. Cosca, H. Masson, J.C. Hunziker, Staircase $^{40}Ar/^{39}Ar$ spectra of fine-grained white mica. Timing and duration of deformation and empirical constraints on argon diffusion, *Geology, 24*, 747-750, 1996.

Kligfield, R., J Hunziker, R.D. Dallmeyer, and S Schamel, Dating of deformation phases using K-Ar and $^{40}Ar/^{39}Ar$ techniques: Results from the northern Appenines, *J. Struct. Geol., 8*, 781-798, 1986.

Koch, P S., J.M. Christie, A. Ord, and R P George Jr., Effect of water on the rheology of experimentally deformed quartzite, *J Geophys. Res., 95*, 13,975-13,996, 1989.

Kronenberg, A.K., Hydrogen speciation and chemical weakening of quartz: in *Silica: Physical Behavior, Geochemistry, and Material Applications, Rev. Mineral.*, vol. 29, edited by P.J. Heaney, C.T. Prewitt and G.V Gibbs, pp. 123-176, Mineral Soc. of Am., Washington, D C., 1994.

Laslett, G. M., P F. Green, I. R. Duddy, and A. J. W., Gleadow, Thermal annealing of fission tracks in apatite, 2, A quantitative analysis, *Chem Geol , 65*, 1-13, 1987.

Law, R.D., Crystallographic fabrics, a selective review of their applications to research in structural geology, in *Deformation Mechanisms, Rheology and Tectonics*, edited by R J Knipe and E.H Rutter, *Geol Soc. Spec. Publ., 54*, 335-352, 1990

Lee, J., Rapid uplift and rotation of mylonitic rocks from beneath a detachment fault: Insights from potassium feldspar $^{40}Ar/^{39}Ar$ thermochronology, northern Snake Range, Nevada, *Tectonics, 14*, 54-77, 1995.

Lee, J., and J.F. Sutter, Incremental $^{40}Ar/^{39}Ar$ thermochronology of mylonitic rocks from the northern Snake Range, Nevada, *Tectonics, 10*, 77-100, 1991.

Lee, J.K.W., T.C. Onstott, K V Cashman, R J. Cumbest, and D Johnson, Incremental heating of hornblende in vacuo: Implications for $^{40}Ar/^{39}Ar$ geochonology and the interpretation of thermal histories, *Geology, 19*, 872-876, 1991

Lister, G.S., and S.L. Baldwin, Modeling the effect of arbitrary P-T-t histories on argon diffusion in minerals using the MacArgon program for the Apple Macintosh, *Tectonophysics, 253*, 83-109, 1996

Lister, G. S., and A W. Snoke, S-C mylonites, *J. Struct. Geol., 6*, 617-639, 1984

Lovera, O.M , Computer programs to model $^{40}Ar/^{39}Ar$ diffusion data from multidomain samples, *Comp. in Geosci., 18*, 789-813, 1992

Lovera, O M., F.M. Richter, and T M Harrison, The $^{40}Ar/^{39}Ar$ thermochronometry for slowly cooled samples having a distribution of domain sizes, *J Geophys. Res., 94*, 17,917-17,935, 1989

Lovera, O.M , F.M Richter, and T.M. Harrison, Diffusion domains determined from ^{39}Ar releases during step heating, *J Geophys Res., 96*, 2,057-2069, 1991

Malavieille, J , Extensional shearing and kilometer-scale "a" type folds in a Cordilleran metamorphic core complex (Raft River Mountains, northwestern Utah), *Tectonics, 6*, 423-448, 1987.

Malavieille, J , Late orogenic extension in mountain belts: Insights from the Basin and Range and the late Paleozoic Variscan belts, *Tectonics, 12*, 1115-1130, 1993.

Malavieille, J., and F. Cobb, Cinematique des deformations ductiles dans trois massifs metamorphiques de l'Ouest des Etats-Unis: Albion (Idaho), Raft River et Grouse Creek (Utah), *Bull. Geol. Soc. Fr., 6*, 885-898, 1986

Manning, A.H., and J.M. Bartley, Postmylonitic deformation in the Raft River metamorphic core complex, northwestern Utah: Evidence of a rolling hinge, *Tectonics, 13*, 596-612, 1994.

McDougall, I., and T.M. Harrison, *Geochronology and Thermochronology by the $^{40}Ar/^{39}Ar$ Method*, 269 pp., Oxford Univ. Press, New York, 1999.

McGrew, A.J., and L.W. Snee, L.W., $^{40}Ar/^{39}Ar$ thermochronolgic constraints on the tectonothermal evolution of the northern East Humboldt Range metamorphic core complex, *Tectonophysics, 238*, 425-450, 1994.

Miller, D. M., R.L. Armstrong, R.R. Compton, and V.R. Todd, Geology of the Albion-Raft River-Grouse Creek Mountains area, northwestern Utah and southern Idaho, *Spec. Stud. Utah Geol. Min. Surv , 59*, 1-59, 1983.

Passchier, C.W., and R.A.J. Trouw, *Microtectonics*, 289 pp., Springer-Verlag, New York, 1996.

Resor, P.G., K.R Chamberlain, C.D. Frost, A.W. Snoke, and B R. Frost, Direct dating of deformation: U-Pb age of syndeformational sphene growth in the Proterozoic Laramie Peak shear zone, *Geology, 24*, 623-626, 1996.

Reuter, A., and R D. Dallmeyer, K-Ar and $^{40}Ar/^{39}Ar$ dating of cleavage formed during very low-grade metamorphism: A review, in *Evolution of Metamorphic Belts*, edited by J.S. Daly, R.A. Cliff, and B.W.D. Yardley, *Geol. Soc. Spec. Publ., 43*, 161-171, 1989.

Richard, S.M., J.E. Fryxell, and J.F. Sutter, Tertiary structure and thermal history of the Harquahala and Buckskin mountains, west central Arizona: Implications for denudation by a major fault system, *J. Geophys. Res., 95*, 19,973-19,987, 1990.

Roeske S M., C. Dusel-Bacon, J.N. Aleinikoff, L.W Snee, and M.A. Lanphere, Metamorphic and structural history of continental crust at a Mesozoic collisional margin, the Ruby Terrane, central Alaska, *J. Met. Geol., 13*, 25-40, 1995.

Ruppel, C , L. Royden, and K.V Hodges, Thermal modeling of extensional tectonics, Application to pressure-temperature-time histories of metamorphic rocks, *Tectonics, 7*, 947-957, 1988.

Sabisky, M. A., Finite strain, ductile flow, and folding in the central Raft River Mountains, northwestern Utah, M.S thesis, 69 pp., Univ. of Utah, Salt Lake City, 1985.

Saltzer, S. D., and K.V Hodges, The Middle Mountain shear zone, southern Idaho· Kinematic analysis of an early Tertiary high-temperature detachment, *Geol Soc Am Bull., 100*, 96-103, 1988.

Samson, S.C , and E C. Alexander Jr., Calibration of the interlaboratory $^{40}Ar/^{39}Ar$ dating standard, MMhb-1, *Chem. Geol., 66*, 27-34, 1987

Scaillet, S., G. Feraud, M Ballevre, and M Amouric, Mg/Fe and [(Mg,Fe)Si-Al2] compositional control on argon behaviour in high-pressure white micas: A $^{40}Ar/^{39}Ar$ continuous laser-probe study from the Dora-Maira nappe of the internal western Alps, Italy, *Geochim Cosmochim. Acta*, 56, 2851-2872, 1992.

Schmid, S.M., and M Casey, Complete fabric analysis of some commonly observed quartz c-axis patterns, in *Mineral and Rock Deformation Laboratory Studies, Geophys Monogr Ser , vol. 36*, edited by B.C. Hobbs and H.C. Heard, pp. 263-296, AGU, Washington, D. C., 1986.

Simpson, C , and D Depaor, Deformation and kinematics of high strain zones, *Short Course Notes*, 116 pp , Geol Soc of Am., Boulder, Colo , 1991.

Snee, L.W., J.F. Sutter, and W C. Kelly, Thermochronology of economic mineral deposits - Dating the stages of mineralization at Panasquira, Portugal, by high precision $^{40}Ar/^{39}Ar$ age spectrum techniques on muscovite, *Econ. Geol., 83*, 335-354, 1988.

Snoke, A W., and D M Miller, Metamorphic and tectonic history of the northeastern Great Basin, in *Metamorphism and Crustal Evolution of the Western United States, Rubey Volume VII*, edited by W G. Ernst, pp 606-648, Prentice-Hall, Englewood Cliffs, N J , 1988

Spencer, J E., and S J. Reynolds, Tectonics of mid-Tertiary extension along a transect through west central Arizona, *Tectonics, 10*, 1204-1221, 1991.

Tagami, T., and C. Shimada, Natural long-term annealing of the zircon fission track system around a granitic pluton, *J. Geophys. Res., 101*, 8245-8255, 1996.

Todd, V. R., Structure and petrology of a Tertiary gneiss complex in northwestern Utah, in *Cordilleran Metamorphic Core Complexes*, edited by M.D. Crittenden, P.J Coney Jr., and G H. Davis, *Mem. Geol. Soc. Am., 153*, 349-383, 1980.

Turner, G., The distribution of potassium and argon in chondrites, in

Origin and Distribution of the Elements, edited by L H Ahrens, pp. 378-398, Pergamon, Tarrytown, N. Y., 1968.

Wells, M.L , Interim geologic map of the Kelton Pass 7 5' quadrangle, Box Elder County, Utah and Cassia County, Idaho, scale 1.12,000 and 1:24,000, *Utah Geol. Surv. Open File Rep 96-342*, 70 pp., 2 plates, 1996.

Wells, M.L., Alternating contraction and extension in the hinterlands of orogenic belts: An example from the Raft River Mountains, Utah, *Geol. Soc. Am. Bull , 109*, 107-126, 1997

Wells, M.L and J R. Struthers, Influence of rheological constraints on mid-crustal extensional shear zone geometry, *Geol. Soc. Am. Abstr Programs, 27*, 283, 1995.

Wells, M.L., T.D. Hoisch, L. Hanson, J Struthers, and E. Wolff, Large magnitude thickening and repeated extensional exhumation in the Raft River, Grouse Creek, and Albion Mountains, *Brigham Young Univ. Geol. Stud., 42*, 325-340, 1997a.

Wells, M.L., J S. Struthers, L.W Snee, A.E. Blythe, and D.M. Miller, Miocene extensional reactivation of an Eocene extensional shear zone, Grouse Creek Mountains, Utah, *Geol Soc. Am. Abstr Programs, 29*, A162, 1997b.

Wernicke, B., and G.J. Axen, On the role of isostacy in the evolution of normal fault systems, *Geology, 16*, 848-851, 1988

White, S., Deformation lamellae in naturally deformed quartz, *Nature, 245*, 26-28, 1973.

Williams, P.L., H.R. Covington, and K.L. Pierce, Cenozoic stratigraphy and tectonic evolution of the Raft River basin, Idaho, in *Cenozoic Geology of Idaho*, edited by B. Bonnichsen and R M. Breckinridge, *Bull Idaho Bur Mines Geol., 26*, 491-504, 1982.

A. E. Blythe, Department of Earth Sciences, University of Southern California, Los Angeles, CA 90089-0740. (blythe@earth.usc.edu)

L. W. Snee, U.S. Geological Survey, Box 25046, MS 974, Federal Center, Denver, CO 80225. (lsnee@crrg1.cr.usgs gov)

M L. Wells, Department of Geoscience, University of Nevada Las Vegas, 4505 Maryland Parkway, Las Vegas, NV 89154-4010. (mlwells@nevada.edu)

(Received February 16, 1999; revised January 29, 2000, accepted March 16, 2000.)